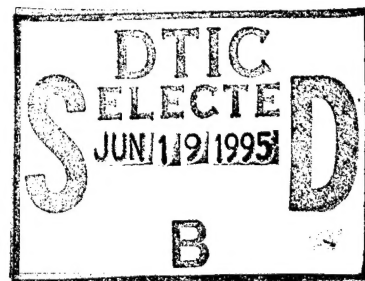


PL-TR-94-2243

REMOTE SOUNDING OF CIRRUS CLOUD PARAMETERS DURING DAYTIME

S.C. Ou
K.N. Liou
N.X. Rao

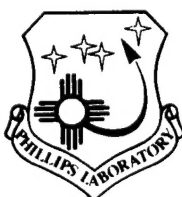
Center for Atmospheric and
Remote Sounding Studies (CARSS)
Department of Meteorology
University of Utah
Salt Lake City, Utah 84112



1 September 1994

Final Report
1 May 1992-1 June 1994

Approved for public release; distribution unlimited





PHILLIPS LABORATORY
DIRECTORATE OF GEOPHYSICS
AIR FORCE MATERIEL COMMAND
HANSCOM AFB, MA 01731-3010


DTIC QUALITY INSPECTED 6

19950615 005

This technical report has been reviewed and is approved for publication.


VINCENT J. FALCONE
Contract Manager


DONALD A. CHISHOLM, Chief
Satellite Analysis and Weather Prediction Branch
Atmospheric Sciences Division


ROBERT A. McCLATCHEY
Director, Atmospheric Sciences Division

This document has been reviewed by the ESC Public Affairs Office (PA) and is releasable to the National Technical Information Service (NTIS).

Qualified requestors may obtain additional copies from the Defense Technical Information Center (DTIC). All others should apply to the NTIS.

If your address has changed, if you wish to be removed from the mailing list, or if the addressee is no longer employed by your organization, please notify PL/IM , 29 Randolph Road, Hanscom AFB, MA 01731-3010. This will assist us in maintaining a current mailing list.

Do not return copies of this report unless contractual obligations or notices on a specific document require that it be returned.

REPORT DOCUMENTATION PAGE			Form Approved OMB No. 0704-0188	
Public reporting burden for this collection of information is estimated to average 1 hour per response, including the time for reviewing instructions, searching existing data sources, gathering and maintaining the data needed, and completing and reviewing the collection of information. Send comments regarding this burden estimate or any other aspect of this collection of information, including suggestions for reducing this burden, to Washington Headquarters Services, Directorate for Information Operations and Reports, 1215 Jefferson Davis Highway, Suite 1204, Arlington, VA 22202-4302, and to the Office of Management and Budget, Paperwork Reduction Project (0704-0188), Washington, DC 20503.				
1. AGENCY USE ONLY (Leave blank)	2. REPORT DATE 1 September 1994	3. REPORT TYPE AND DATES COVERED Final Report, 1 May 1992 - 1 June 1994		
4. TITLE AND SUBTITLE Remote Sounding of Cirrus Cloud Parameters during Daytime		5. FUNDING NUMBERS F 19628-92-K-0019 PE 61102F PR 2310 TR CP WU KA		
6. AUTHOR(S) S.C. Ou, K.N. Liou, and N.X. Rao				
7. PERFORMING ORGANIZATION NAME(S) AND ADDRESS(ES) Center for Atmospheric and Remote Sounding Studies (CARSS) Department of Meteorology University of Utah, Salt Lake City, Utah 84112		8. PERFORMING ORGANIZATION REPORT NUMBER		
9. SPONSORING/MONITORING AGENCY NAME(S) AND ADDRESS(ES) Phillips Laboratory 29 Randolph Road Hanscom AFB, MA 01731-3010 Contract Manager: Vincent Falcone/GPAB		10. SPONSORING/MONITORING AGENCY REPORT NUMBER PL-TR-94-2243		
11. SUPPLEMENTARY NOTES				
12a. DISTRIBUTION/AVAILABILITY STATEMENT Approved for public release; distribution unlimited		12b. DISTRIBUTION CODE		
13. ABSTRACT (Maximum 200 words) A numerical scheme has been developed to remove the solar component in the AVHRR 3.7 μm channel for the retrieval of cirrus parameters during daytime. The cloud retrieval scheme described in Ou et al. (1993) has been modified in connection with the removal program. We have applied the removal-retrieval scheme to the AVHRR daytime data, collected during FIRE-I-IFO. Distributions of the retrieved cloud heights and optical depths are comparable to those determined from lidar measurements and from GOES visible and IR channels data reported by Minnis et al. (1990a). Moreover, validation of the algorithm has been performed by using various data sets that were collected during the FIRE-II-IFO (November -December, 1991) at Coffeyville, Kansas. We have focused on the 5 December case. We demonstrate that the retrieved cirrus cloud temperature, mean effective ice crystal size, and optical depth closely match the values derived from the balloon-borne replicator measurements.				
14. SUBJECT TERMS Cirrus clouds, remote sensing, AVHRR		15. NUMBER OF PAGES 68		
		16. PRICE CODE		
17. SECURITY CLASSIFICATION OF REPORT Unclassified	18. SECURITY CLASSIFICATION OF THIS PAGE Unclassified	19. SECURITY CLASSIFICATION OF ABSTRACT Unclassified	20. LIMITATION OF ABSTRACT Unlimited	

TABLE OF CONTENTS

	<u>Page</u>
1. INTRODUCTION.....	1
2. REMOVAL-RETRIEVAL SCHEME	5
2.1 Detection of Clear and Cloudy Pixels	5
2.2 Removal of 3.7 μm Solar Component	7
2.3 Retrieval of Cirrus Cloud Parameters	15
2.4 Removal-Retrieval Scheme	18
3. SENSITIVITY STUDIES AND ERROR ANALYSES	21
4. APPLICATION TO SATELLITE DATA ASSOCIATED WITH FIRE-I-IFO	32
4.1 Retrieval over a 1° x 1° Area	34
4.2 Retrievals over a 5° x 5° Area	39
4.3 Retrievals over a 20° x 30° Area	44
5. VERIFICATION USING FIRE-II-IFO MEASUREMENTS	50
5.1 Data Sources	50
5.2 Results and Discussions	51
6. CONCLUSIONS	60
REFERENCES	62

By _____	
Distribution/ _____	
Availability Codes	
Dist	Avail and/or Special
A-1	

1. INTRODUCTION

Cirrus clouds are global in nature and primarily exist in the upper troposphere and lower stratosphere. These clouds are composed almost entirely of ice crystals. Cirrus clouds play a key role in the global energy balance through latent heat and radiative energy exchanges. Information on cirrus cloud parameters is critically important to the development of cirrus forecast models, and the upgrading of real-time global cloud analysis (Liou 1986).

Inference of the microphysical and optical properties of cirrus clouds using satellite or aircraft data has been reported by a number of researchers. Wielicki et al. (1990) used the Landsat 0.83, 1.65, and 2.21 μm channel reflectances and phase functions for ice crystals to infer cirrus cloud particle sizes, assuming that single scattering dominates the radiative transfer within cirrus clouds. Liou et al. (1990) developed a physical retrieval method to infer the temperature and optical depth of tropical cirrus anvils using the data of the dual channel (6.5 and 10.5 μm), downward-viewing, narrow-field-of-view radiometers on board NASA ER-2. Minnis et al. (1993a, b) developed a technique based on the radiative transfer theory and parameterizations to retrieve cirrus optical depth and height using the Geostationary Operational Environmental Satellite (GOES) 0.65 and 11.5 μm channel radiances. Ou et al. (1993) presented a physical retrieval scheme using the Advanced Very High-Resolution Radiometer (AVHRR) 3.7 and 10.9 μm channels for the inference of nighttime cirrus cloud parameters, including cloud temperature, optical depth, emissivity, and mean effective ice crystal size based on the theory of radiative transfer and parameterizations. This retrieval scheme has been applied to the nighttime AVHRR satellite data collected at 0930 UTC, 28 October, 1986, over the region of the First ISCCP Regional Experiment, Phase I, Cirrus Intensive Field Observation (FIRE-I-IFO). The retrieved cirrus height and mean effective ice crystal size compare reasonably well with ground-based lidar and aircraft measurements.

During daytime, the 3.7 μm channel radiance contains both solar reflection and thermal emission. To apply the retrieval scheme to the daytime satellite data, the 3.7 μm channel solar component must be quantified and removed. The problem of removing the 3.7 μm solar reflection (referred to as "sol") and thermal infrared emission (referred to as "IR") component for remote sensing applications has been investigated by several researchers in the past. Arking and Childs (1985) included the solar component of the 3.7 μm channel in the formulation of a general retrieval program for cloud parameters. Kleespies (1993) proposed a dual-observation method to remove the thermal infrared component in the 3.7 μm channel radiances for inferring the particle sizes of opaque marine stratiform clouds. In this report, we describe a method to remove the solar component in the AVHRR 3.7 μm channel radiance for the retrieval of cirrus cloud parameters during daytime. This method involves various threshold values for AVHRR Chs. 1 (0.63 μm), 2 (0.8 μm), 3 (3.7 μm), 4 (10.9 μm), and 5 (12 μm), which are prescribed to separate clear and cloudy pixels. A look-up table relating the Ch. 1 reflectance to the Ch. 3 solar reflectance is subsequently constructed. This table is based on the effective surface albedos, selected ice crystal sizes, and a set of sun-satellite geometric parameters. A comprehensive adding-doubling radiative transfer program is used to generate numerical values in the look-up table. Removal of the Ch. 3 solar component is accomplished by using the look-up table and the measured Ch. 1 reflectance. For retrieval of cloud parameters during daytime, the scheme described in Ou et al. (1993) is modified in connection with the removal program.

Validation of the satellite remote sensing technique for the retrieval of cirrus cloud parameters requires ground and air-truths that are available from a composite field experiment. In addition to our efforts cited above, Minnis et al. (1990b; 1993b) have used ground-based lidar measurements collected during FIRE-I-IFO to verify the retrieved cirrus cloud height. Baum et al.

(1994) have also presented comparison results for the satellite retrieved and lidar, radar, and aircraft-measured cloud heights, using data collected during FIRE-II-IFO. However, attempt to validate the retrieved optical depths and ice crystal sizes using aircraft data has not been made at this point. The prime difficulties for this are due to the horizontal nature of aircraft flight path and the inhomogeneity of cirrus cloud properties. To evaluate the cirrus cloud vertical optical depth, continuous microphysical measurements in the vertical must be available. Moreover, to minimize the effects of horizontal inhomogeneity, the cloudy region sampled by the in-situ instruments must correspond to that viewed by the satellite.

We have carried out a more comprehensive validation for the retrieved cirrus cloud optical depths and mean effective ice crystal sizes, using the NOAA-11 AVHRR data, the balloon-borne replicator data, and the NCAR-CLASS (Cross-chain LORAN Atmospheric Sounding System) sounding measurements that were obtained during FIRE-II-IFO. The advantage of using the replicator data is that the replicator sondes will provide a continuous record of the cloud microphysical properties in the vertical. Thus, it is possible to determine the optical depth and vertically averaged mean effective ice crystal size. Furthermore, we have also used the retrieved cirrus cloud optical depths and mean effective ice crystal sizes in conjunction with a radiative transfer parameterization program to compute the surface radiative fluxes which are subsequently compared with the ground-based radiometer measurements that were obtained during FIRE-II-IFO. These comparisons will thus provide a consistent check on the retrieved cloud parameters, on the one hand, and the radiation parameterization program, on the other.

This report is organized as follows. Section 2 describes the clear/cloud detection scheme and the removal-retrieval procedures. Section 3 presents the results of sensitivity studies and discusses the effects of various possible

error sources on the accuracy of removal-retrieval results. In Section 4, we demonstrate the applicability of the retrieval algorithm to satellite data associated with FIRE-I-IFO. Section 5 then presents results of a validation effort using data obtained from two cases of FIRE-II-IFO. Finally, conclusions are given in Section 6.

2. REMOVAL-RETRIEVAL SCHEME

2.1 Detection of Clear and Cloudy Pixels

The clear/cloud detection scheme is based on several criteria described in Saunders and Kriebel (1988). Figure 1 presents a schematic flow chart of the detection scheme for identifying clear pixels during daytime. The first criterion involves the use of the Ch. 4 brightness temperature (T_4). For a clear pixel, T_4 must be greater than a defined threshold temperature (T_{4C}). We may use the map of T_4 over the clear portion of the data domain to derive a mean clear brightness temperature (\bar{T}_4). The T_{4C} is empirically set as $\bar{T}_4 - 2$ K. Pixels that satisfy the first criterion subsequently undergo the second test, which requires that the Ch. 1 reflectance (r_1) be smaller than a threshold value (r_{1C}), i.e. $r_1 < r_{1C}$. The threshold r_{1C} is determined based on the identification of peaks corresponding to cloudy and clear conditions in the histogram of r_1 .

Clouds generally have high reflectances, whereas most types of ground and sea surfaces (except snow and ice) have low reflectances at the visible wavelengths. Using this property, a visible threshold may be set up to differentiate between cloudy and clear reflectances. Because the clear reflectance varies with the surface type, the visible threshold is a function of surface characteristics. The third criterion uses the ratio of Ch. 2 ($0.8 \mu\text{m}$) to Ch. 1 ($0.63 \mu\text{m}$) reflectances ($Q = r_2/r_1$). This ratio has a unique feature with respect to surface types. For clouds, Q is closer to 1 because the cloud reflectances for these two wavelengths are about the same. Over water surfaces, $Q < 1$ because the reflectance of the $0.63 \mu\text{m}$ wavelength is more pronounced. Over land with vegetation, $Q \gg 1$ because the reflectance at the $0.8 \mu\text{m}$ wavelength is much larger than that at the $0.63 \mu\text{m}$ wavelength. We define a threshold value Q_c such that a pixel is clear if $Q > Q_c$. We have set a uniform value of 1.6 (corresponding to land). This threshold value is applied to all the present retrieval analyses, because most of the area within the retrieval domains are

Daytime Clear/Cloud Detection Scheme

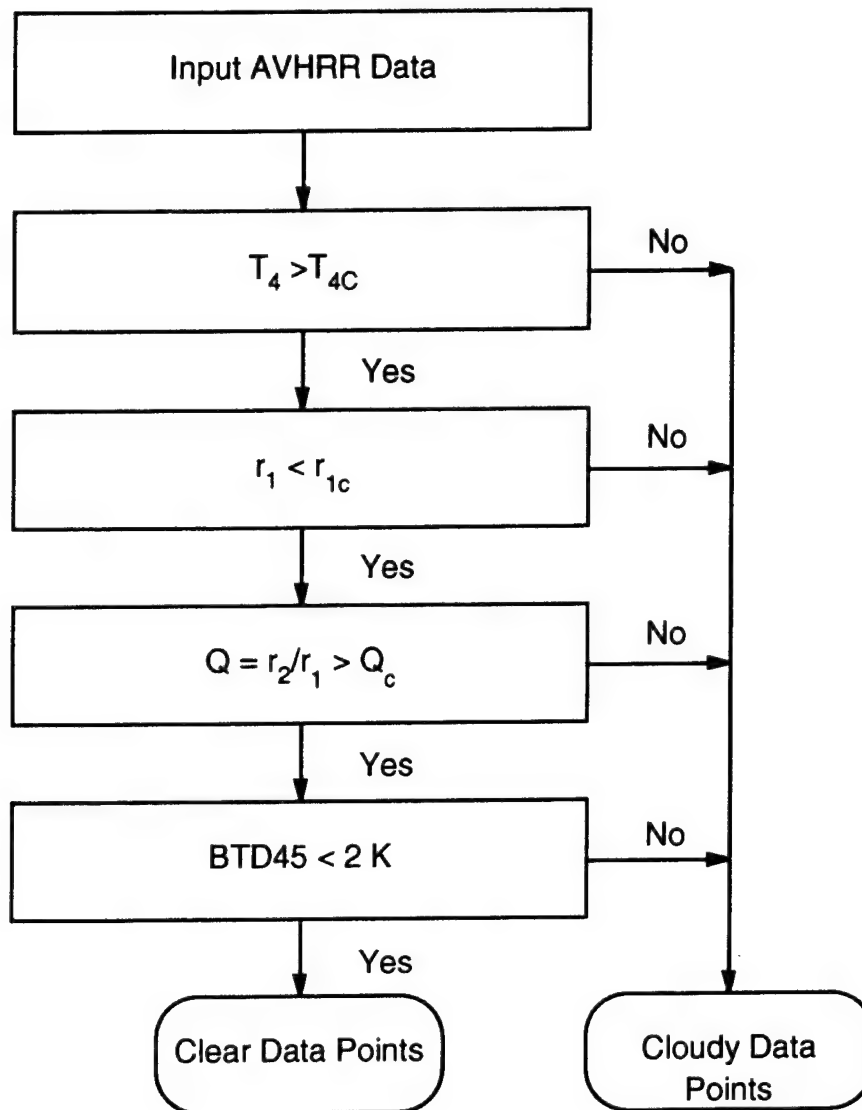


Fig 1. A flow chart for the daytime clear/cloud detection scheme.

over land. The only significant water surfaces involved are over the Great Lake region. However, the display of Ch. 4 brightness temperatures shows that this area is mostly cloudy. Pixels over that area are identified as cloudy by other criteria (see Section 4.c). Finally, the fourth criterion uses the difference between Ch. 4 and Ch. 5 brightness temperatures which must be less than a threshold value, δ (~ 2 K). If a pixel satisfies all four criteria, it is identified as clear. Otherwise, it is classified as cloudy. These criteria are complementary to each other. For example, low-cloud pixels are identified as cloudy because their Ch. 1 reflectances are higher than the threshold (criterion 2), even though their brightness temperature difference between Chs. 4 and 5 is smaller than 2K (criterion 4). Also, pixels associated with thin cirrus are identified as cloudy as long as their Ch. 4 brightness temperatures are lower than the threshold value (criterion 1), even though their Ch. 1 reflectances and brightness temperature differences are lower than threshold values.

2.2 Removal of 3.7 μm Solar Component

Let the angle of the incident solar radiation be θ_0 , while the satellite viewing angle be θ . The relative azimuthal angle ($\Delta\phi$) is defined as the angle between the horizontal projection planes of the sun and the satellite. We define μ_0 and μ to be the cosines of the solar and satellite zenith angles, respectively. Moreover, let the Chs. 1 and 3 solar reflectances in the direction of $(\mu, \Delta\phi)$ for cirrus cloudy conditions be $r_1(\mu_0, \mu, \Delta\phi)$ and $r_3(\mu_0, \mu, \Delta\phi)$, respectively, which can be evaluated from the following parametric equation (Liou, 1980, p. 216; Arking and Childs, 1985):

$$r_i(\mu_0, \mu, \Delta\phi) = r_i^*(\mu_0, \mu, \Delta\phi) + \frac{\gamma_i(\mu)\gamma_i(\mu_0)r_{ai}}{1 - r_{ai}\bar{r}_i}, \quad i = 1, 3, \quad (1)$$

where $r_i^*(\mu_0, \mu, \Delta\phi)$ are the solar reflectances due to cloud layer only, \bar{r}_i are the albedo of the cloud layer, and r_{ai} are the effective surface albedos that take

into account the Rayleigh scattering effects in the visible spectral region and the water vapor absorption effects in the near IR region. Moreover, $\gamma_i(\mu)$ and $\gamma_i(\mu_0)$ are the total directional transmittances in the direction of $(\mu, \Delta\phi)$ and $(\mu_0, 0)$, respectively. These transmittances are composed of direct and diffuse transmittances of the incoming radiation as follows:

$$\gamma_i(\mu) = e^{-\tau_i/\mu} + t_i(\mu), \quad (2)$$

where τ_i are the optical depths for Chs. 1 and 3, and t_i are given by

$$t_i(\mu) = \frac{1}{\pi} \int_0^{2\pi} \int_0^1 t_i^*(\mu', \mu, \Delta\phi) \mu' d\mu' d(\Delta\phi), \quad (3)$$

where $t_i^*(\mu', \mu, \Delta\phi)$ are the downward transmitted diffuse radiance in the direction μ for Chs. 1 and 3, and F_{0i} are the respective incident solar irradiances. The albedo of clouds can be obtained from the following (Liou, 1980, p. 202):

$$\bar{r}_i = 2 \int_0^1 r_i'(\mu) \mu d\mu, \quad (4)$$

where $r_i'(\mu)$ is defined similarly to Eq. (3). Finally, the second term in Eq. (1) represents the fraction of incoming solar radiation that is reflected to the satellite due to multiple reflections between the surface and the cloud base.

We develop a look-up table relating $r_1(\mu_0, \mu, \Delta\phi)$ and $r_3(\mu_0, \mu, \Delta\phi)$ based on Eq. (1) for different satellite viewing geometries and cirrus cloud optical and microphysical properties. In Figure 2, the procedures for the construction of such a look-up table for removing the 3.7 μm solar radiance are outlined. We first estimate the mean Ch.1 effective surface albedo, r_{a1} , using satellite data. Once clear pixels are identified via the preceding detection scheme, the angular dependent Ch.1 solar reflectance, $r_1(\mu_0, \mu, \Delta\phi)$, for each clear pixel is computed from the satellite data, $\bar{r}_1(\mu, \Delta\phi)$, which has been normalized with respect to the incident solar radiation in the zenith direction as follows:

Construction of Look-up Table Correlating Chs. 1 and 3 Reflectances

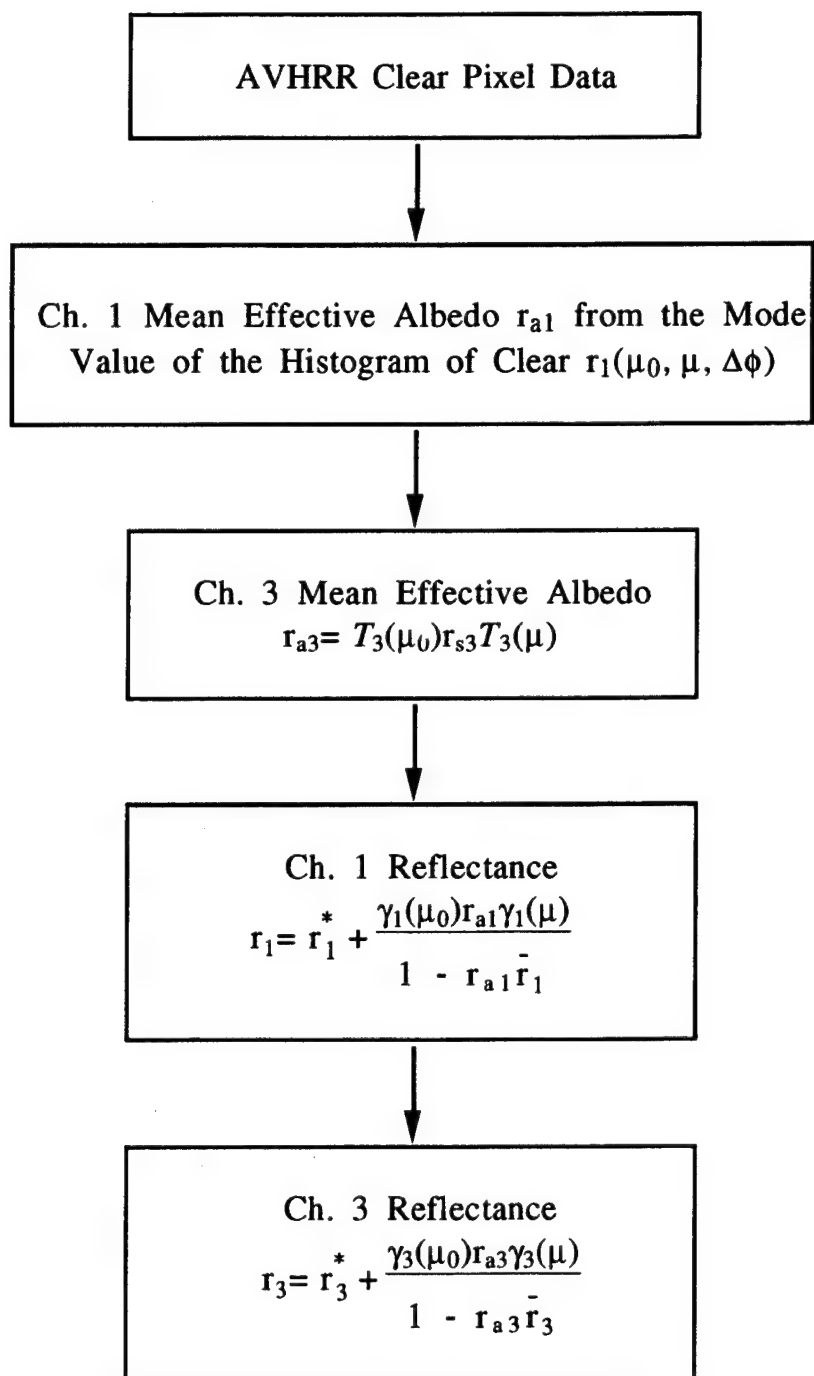


Fig 2. A flow chart for the construction of a look-up table involving the correlation between Ch. 1 and Ch. 3 solar reflectances.

(5)

$$r_1(\mu_0, \mu, \Delta\phi) = \tilde{r}_1(\mu, \Delta\phi)/\mu_0.$$

Subsequently, we construct a one-dimensional histogram of $r_1(\mu_0, \mu, \Delta\phi)$ for all clear pixels, and directly estimate r_{a1} from the peak value of the histogram. This procedure will yield reasonable values of r_{a1} , because the Ch. 1 clear radiance contains the effects of Rayleigh scattering.

The preceding procedure is not applicable to evaluating the Ch. 3 effective surface albedo, r_{a3} , since the Ch. 3 clear radiance contains both solar and thermal infrared components. The magnitude of the thermal infrared component is generally unknown. To estimate r_{a3} , we use the following formula based on the radiative transfer principle:

$$r_{a3} = T_3(\mu_0) r_{s3} T_3(\mu), \quad (6)$$

where $T_3(\mu)$ is the total atmospheric transmittance in the direction of μ , and r_{s3} is the Ch. 3 surface albedo. The three terms in Eq. (6) represent downward atmospheric transmission, surface reflection, and upward atmospheric transmission of solar radiation, respectively. Since the effects of Rayleigh scattering on the transfer of the $3.7 \mu\text{m}$ wavelength are relatively weak, multiple reflections between the surface and the Rayleigh layer are neglected in Eq. (6). Based on calculations using the LOWTRAN program and the U.S. Standard Atmosphere Profile (Handbook of Geophysics, 1985), the atmospheric transmittance between 3.6 and $4.0 \mu\text{m}$ is on the order of 0.85 - 0.90 .

The exact value of r_{s3} is also unknown. However, from laboratory measurements (Sutherland, 1986) the $3.7 \mu\text{m}$ surface emissivity varies between 0.8 and 1.0 for several types of natural soil and vegetation. Thus, the surface albedo, r_{s3} , has a value between 0.0 and 0.2 based on Kirchhoff's law. Bunting and Hardy (1974) presented an average r_{s3} value of 0.15 for the snow-free land. Allen et al. (1990) reported that for snow, r_{s3} depends on the snow grain size and varies between 0.005 and 0.025 . Based on the preceding values, r_{s3} is set

as 0.1 in the present removal scheme. Once the effective surface albedos for Chs. 1 and 3 are determined, we then proceed to compute the solar reflectances of the two channels following Eq. (1). For this purpose, we compute the single-scattering properties based on the measured ice crystal size distributions. Details of this step are described in the following.

We have analyzed six composite ice crystal size distributions that were obtained from the data presented by Heymsfield and Platt (1984), Takano and Liou (1989a), and the FIRE-I-IFO microphysic data. They are denoted as Cold Ci, -60°C, Cs, FIRE-I-IFO Nov. 1, FIRE-I-IFO Nov. 2, and Ci Uncinus. We first define a mean effective width (or size) to represent ice-crystal size distribution in the form

$$D_e = \frac{\int_{L_{\min}}^{L_{\max}} D^2 \ln(L) dL}{\int_{L_{\min}}^{L_{\max}} D \ln(L) dL}, \quad (7)$$

where D and L denote the width and the maximum dimension of a nonspherical ice crystal, respectively, and $n(L)$ is the size distribution in terms of L . The rationale for defining D_e to represent ice crystal size distribution is that the scattering of light is related to the geometric cross section, which is proportional to LD . Light scattering and absorption programs developed by Takano and Liou (1989a) for hexagonal ice crystals have been used to compute single-scattering properties as functions of D_e . To compute D_e , we use the empirical relationship of L and D based on laboratory data (Auer and Veal, 1970):

$$D = aL^b, \quad (8)$$

where a and b are empirical coefficients. Each size distribution is discretized into five intervals, and D_e is computed by summation of the integrands in Eq. (7). The single-scattering albedos ($\bar{\omega}$), phase functions, and extinction coefficients ($\bar{\beta}_e$) for a given ice crystal size distributions are computed from

the following equations:

$$\bar{\omega} = \int_{L_{\min}}^{L_{\max}} \beta_s n(L) dL / \int_{L_{\min}}^{L_{\max}} \beta_e n(L) dL, \quad (9)$$

$$\bar{P}(\theta) = \int_{L_{\min}}^{L_{\max}} P(\theta) \beta_s n(L) dL / \int_{L_{\min}}^{L_{\max}} \beta_s n(L) dL, \quad (10)$$

$$\bar{\beta}_e = \int_{L_{\min}}^{L_{\max}} \beta_e n(L) dL, \quad (11)$$

where β_s and β_e are the scattering and extinction cross sections, respectively, and $P(\theta)$ is the phase function as a function of the scattering angle θ . Table 1 lists the values of D_0 , $\bar{\omega}$, \bar{g} , and $\bar{\beta}_e$ for six measured ice crystal size distributions, whose \bar{g} is the asymmetry factor associated with the phase function. For $0.63 \mu\text{m}$, $\bar{\omega}$ is very close to 1 for all D_0 s, while for $3.7 \mu\text{m}$, $\bar{\omega}$ decreases from 0.79 for the smallest D_0 to 0.59 for the largest D_0 . Moreover, \bar{g} for both wavelengths increases with D_0 . The implication of these behaviors in the removal of the $3.7 \mu\text{m}$ solar component will be discussed in the following.

The single-scattering parameters for hexagonal ice columns/plates (Takano and Liou, 1989a) are used in the adding-doubling radiative transfer program developed by Takano and Liou (1989b) to compute $r_1^*(\mu_0, \mu, \Delta\phi)$, $\gamma_1(\mu)$, $\gamma_1(\mu_0)$, and \bar{r}_1 . This ice crystal model is the best we have so far. The effects of ice crystal shapes on the single-scattering properties as they pertain to remote sensing applications is a subject requiring further investigations. In the computations, we use 10 optical depths ranging from 0.125 to 64. Figure 3 shows an example of the relationship between the reflectances r_3 and r_1 for the six ice crystal size distributions and the prescribed viewing geometry. Numbers in parentheses are D_0 values. Values of effective surface albedos for Chs. 1 and 3, r_{a1} and r_{a3} , are specified to be 0.12 and 0.046, respectively. It is noted that radiances of both channels converge to the values of r_{a1} and r_{a3} for thin cirrus. Reflectance r_3 reaches asymptotic values for $r_1 > 0.4$ due to saturated

Table 1. Single scattering properties for six composite measured size distributions, where D_e is the mean effective ice crystal size, $\bar{\beta}_e$ is the extinction coefficient, $\bar{\omega}$ is the single scattering albedo, and \bar{g} is the asymmetry factor.

Cirrus Type	$D_e(\mu\text{m})$	0.63 μm			3.7 μm		
		$\bar{\beta}_e(\text{km}^{-1})$	$\bar{\omega}$	\bar{g}	$\bar{\beta}_e(\text{km}^{-1})$	$\bar{\omega}$	\bar{g}
Cold Ci	23.9	0.16623	0.999997	0.77125	0.16620	0.79166	0.80632
-60°C	30.4	0.07596	0.999996	0.77565	0.07596	0.76369	0.82345
Cs	41.5	0.38650	0.999995	0.78367	0.38653	0.71298	0.85821
FIRE-I Nov. 1	75.1	0.20209	0.999990	0.81659	0.20210	0.63263	0.91367
FIRE-I Nov. 2	93.0	0.44736	0.999988	0.83065	0.44736	0.60636	0.93561
Ci Uncinus	123.6	2.60580	0.999984	0.83966	2.60580	0.58885	0.93561

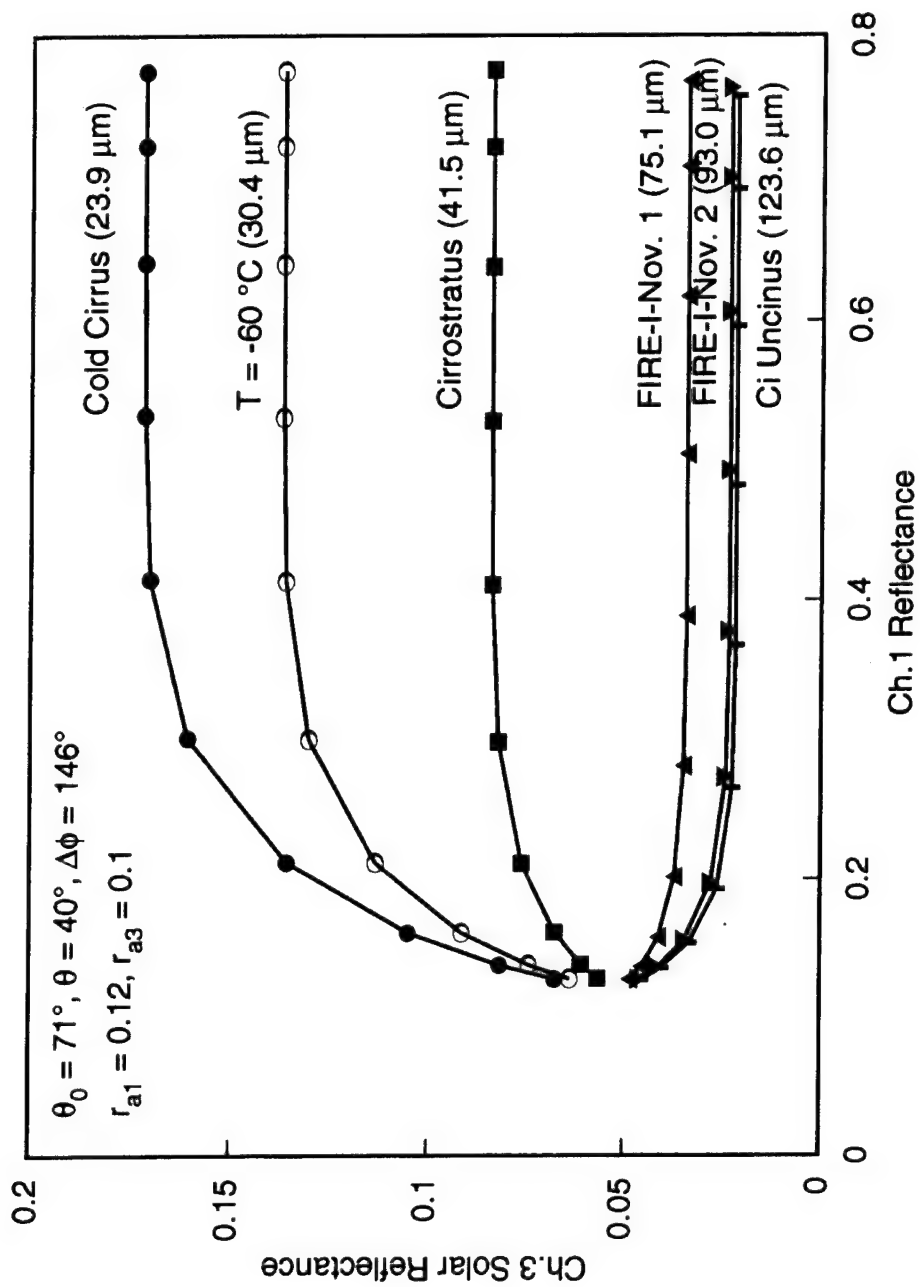


Fig 3. Correlations between the Ch. 3 solar reflectance (r_3) and Ch. 1 reflectance (r_1) for six measured ice crystal size distributions.

absorption by clouds with large optical depth. Moreover, this asymptotic value decreases with increasing D_e , because $\bar{\omega}$ decreases with increasing D_e and \bar{g} increases with increasing D_e . The preceding analyses have the following implications. First, the removal of $3.7 \mu\text{m}$ solar component depends on the values of r_{a1} and r_{a3} for thin cirrus clouds. However, this dependence becomes less significant for $r_1 > 0.4$. Thus, it is important to specify the values of r_{a1} and r_{a3} as accurate as possible if thin cirrus clouds are involved. We may improve the initial guess for r_{a3} by determining r_{s3} from the information of surface land type. Second, for $r_1 > 0.4$, r_3 depends on D_e only. Thus, it is possible to estimate r_3 , T_c , and D_e directly from Chs. 1, 3, and 4 radiances for thick cirrus. Finally, for $D_e > 100 \mu\text{m}$, r_3 is independent of D_e as it approaches a minimum value of ~ 0.02 for the present set of geometric parameters.

Once the look-up correlation table is established, the solar component in the $3.7 \mu\text{m}$ radiances is removed with the aid of the $0.63 \mu\text{m}$ reflectance and a trial mean effective ice crystal size. After this removal, the remaining thermal infrared radiance of $3.7 \mu\text{m}$ coupled with the $10.9 \mu\text{m}$ radiance is used to perform retrieval using the program developed by Ou et al. (1993) to obtain the cirrus cloud temperature, mean effective ice crystal size (from cloud temperature), and emissivity. A brief overview of the retrieval methodology is given in the next section.

2.3 Retrieval of Cirrus Cloud Parameters

The retrieval methodology follows the principles of the dual thermal infrared channel technique presented in Liou et al. (1990) and Ou et al. (1993). The retrieval of cirrus cloud parameters is based on the numerical solution of the following set of nonlinear algebraic equations derived from the theory of radiative transfer and parameterizations:

$$R_i = R_{ai}(1 - \epsilon_i) + \epsilon_i B_i(T_c), \quad (12)$$

$$\epsilon_i = 1 - \exp(-k_i \tau), \quad i = 3, 4, \quad (13)$$

$$B_3(T_c) = \sum_{n=0}^3 a_n [B_4(T_c)]^n, \quad (14)$$

where R_i are the upwelling thermal infrared radiances at the top of the atmosphere for Chs. 3 and 4 over cirrus clouds, R_{ai} are the corresponding thermal infrared radiances reaching the cloud base for the two channels, ϵ_i are the cloud emissivities, T_c is the equivalent radiating cirrus temperature, $B_i(T_c)$ are the Planck intensities at T_c , τ is the visible optical depth (simply referred to as optical depth), and k_i are the adjustment factors to account for scattering and wavelength difference, referred to as the effective extinction coefficients. Polynomial form is used to relate $B_3(T_c)$ and $B_4(T_c)$ in Eq. (14). Because both $B_3(T_c)$ and $B_4(T_c)$ are smooth functions of T_c , polynomial fitting of these values gives very small errors (< 1%). The values of polynomial coefficients are $a_0 = 2.6327 \times 10^{-4}$, $a_1 = -1.063 \times 10^{-4}$, $a_2 = -8.2976 \times 10^{-6}$, and $a_3 = 3.7311 \times 10^{-7}$.

The solution involves the effective extinction ratio for the two channels, k_4/k_3 , which is dependent on D_0 . To investigate the dependence of the effective extinction ratio on D_0 , we have used the light scattering and radiative transfer program developed by Takano and Liou (1989a, b) to compute k_4/k_3 as a function of D_0 . Table 2 shows the dependence k_4/k_3 on D_0 based on 12 measured size distributions (Ou et al., 1993). The value of k_4/k_3 increases as D_0 becomes smaller, implying that more scattering is associated with the $3.7 \mu\text{m}$ wavelength than $10.9 \mu\text{m}$. Thus, it is necessary to know D_0 in order to compute k_4/k_3 . In the dual-channel technique ($6.5 \mu\text{m}$ and $10.5 \mu\text{m}$) developed by Liou et al. (1990), information of the ice crystal size is not required because the dependence of the emissivity on the size is negligible in these two wavelengths. A second-degree

polynomial least-square fitting for this ratio in terms of $1/D_e$ has been developed:

$$k_4/k_3 = \sum_{n=0}^2 b_n D_e^{-n}. \quad (15)$$

where $b_0 = 0.722$, $b_1 = 55.08$, and $b_2 = 174.12$.

Based on a large number of cirrus microphysical data collected by optical probes during flights over midlatitudes, Heymsfield and Platt (1984) have developed a functional form for the measured ice crystal size distribution using a general power form as follows:

$$n(L) = \begin{cases} A_1 L^{B_1}(\text{IWC}), & L \leq L_0, \\ A_2 L^{B_2}(\text{IWC}), & L > L_0, \end{cases} \quad (16)$$

where $L_0 = (A_2/A_1)^{1/(B_1-B_2)}$; IWC is the ice water content; which can be parameterized as a function of temperature (Liou 1992) and $A_{1,2}$ and $B_{1,2}$ are temperature-dependent coefficients determined from the measured data. Table 3 lists the values of constants in Eq. (16). According to this parameterization, D_e is a function of temperature. We perform a least-square polynomial fitting to relate D_e to cloud temperature (T_c) in the form

$$D_e = \sum_{n=0}^3 c_n (T_c - 273)^n, \quad (17)$$

where $c_0 = 326.3$, $c_1 = 12.42$, $c_2 = 0.197$, and $c_3 = 0.0012$. From this equation, D_e increases with increasing T_c , which is consistent with recent aircraft microphysics measurements reported by Heymsfield et al. (1990).

In order to solve Eqs. (12)-(14), the upwelling radiances reaching the cloud base, R_{ai} , must be given. They are determined by using the radiances of clear pixels, because very little water vapor is present above cirrus clouds. It follows that if we can identify the clear pixels, R_{ai} may be determined by a

Table 2 Values of the effective extinction ratio k_4/k_3 as a function of the mean effective size D_e . Values of D_e are computed from a number of measured ice-crystal size distributions.

$D_e (\mu m)$	k_4/k_3
23.9	2.725
30.4	2.364
41.5	1.792
47.5	1.908
57.9	1.705
64.1	1.585
75.1	1.347
93.0	1.231
104.1	1.242
106.7	1.224
110.4	1.212
123.6	1.182

statistical method. We may select a scene and use the data within this scene to construct a two-dimensional histogram in the domain of R_3 and R_4 . The radiances corresponding to the peak of the frequency distribution are assigned as the mean clear radiances. The area of the scene should be large enough to contain a statistically significant amount of pixels. At the same time, this area should also be sufficiently small to guarantee the homogeneity of the surface temperature and water vapor distributions within the scene. Ou et al. (1993) used the FIRE-I-IFO data and two sizes ($1^\circ \times 1^\circ$) and ($0.5^\circ \times 0.5^\circ$) to investigate the effects of varying the area size on the retrieval and found that the variability of the clear radiances decreases with decreasing size of the area. However, the mean clear radiances remain unchanged. Both Minnis et al. (1993b) and Chou (1991) used the ISCCP grid ($2.5^\circ \times 2.5^\circ$) for the determination of clear radiances.

2.4 Removal-Retrieval Scheme

Both the removal and retrieval programs are dependent on the ice crystal size distribution represented by the mean effective size, D_e . The mean effective

Table 3. Values of A_1 , A_2 , B_1 , B_2 , L_0 , and IWC in Eq. (16) as functions of temperature.

Temperature (°C)	A_1	A_2	B_1	B_2	L_0 (μm)	IWC (g/m^3)
-20 ~ -25	6.837×10^8	3.304×10^{12}	-2.56	-3.74	977	0.0270
-25 ~ -30	7.328×10^8	3.068×10^{14}	-2.51	-4.49	691	0.0250
-30 ~ -35	1.954×10^8	9.063×10^{12}	-2.21	-3.94	498	0.0175
-35 ~ -40	7.540×10^8	1.329×10^{14}	-2.29	-4.37	333	0.0126
-40 ~ -45	2.163×10^{12}	—————	-3.23	—————	———	0.0034
-45 ~ -50	1.117×10^{11}	—————	-3.15	—————	———	0.0025
-50 ~ -55	1.778×10^{11}	—————	-3.83	—————	———	0.0018
-55 ~ -60	2.800×10^{11}	—————	-3.85	—————	———	0.0009

sizes are computed on a pixel-by-pixel basis. They are determined from the retrieved cloud temperature based on the relationship between the mean effective size and cloud temperature (Eq. 17) and not selected out of the six measured size distributions presented in Figure 3. A value of $D_e^{(0)}$ is prescribed initially. This value is usually the largest possible value of D_e , which corresponds to the minimum amount of solar radiances to be removed. Using satellite-derived r_{a1} , and prescribed r_{s3} , a look-up table for r_3 versus r_1 is constructed according to the procedures described in Section 2.2. The solar reflectance r_3 is then obtained from the measured $0.63 \mu\text{m}$ reflectance and the look-up table. Let the reflected radiance of Ch. 3 be $R_{3\text{sol}}$. Thus,

$$R_{3\text{sol}} = \mu_0 F_{03} r_3, \quad (18)$$

where F_{03} is the incident solar irradiance, which is obtained from Thekaekara (1974), and r_3 is the solar reflectance for the $3.7 \mu\text{m}$ channel. Let the thermal infrared component of Ch. 3 be $R_{3\text{ir}}$. The initial value for $R_{3\text{ir}}$ is obtained from the following

$$R_{3ir}^{(0)} = R_3 - R_{3sol}^{(0)}. \quad (19)$$

Both $R_{3ir}^{(0)}$ and R_4 [Eq. (12)] are used in the cirrus retrieval program. The same $D_e^{(0)}$ as in the removal scheme is utilized to specify k_4/k_3 according to Eq. (15). A new cirrus cloud temperature $T_c^{(0)}$ is then obtained. From $T_c^{(0)}$, we may compute an intermediate value for $\tilde{D}_e^{(1)}$, using Eq. (17). Because we have removed the minimum amount of the $3.7 \mu m$ solar component, the thermal infrared component $R_{3ir}^{(0)}$ will be overestimated based on Eq. (19). From Eqs. (12) and (17), $T_c^{(0)}$ and $\tilde{D}_e^{(1)}$ will be underestimated. Thus, the difference $|\tilde{D}_e^{(1)} - \tilde{D}_e^{(0)}|$ would be substantial. If we apply $\tilde{D}_e^{(1)}$ to the removal-retrieval scheme, numerical instability may occur. To avoid this, a new suppressed value of $D_e^{(1)}$ is computed as follows:

$$D_e^{(1)} = \alpha \tilde{D}_e^{(1)} + (1-\alpha) D_e^{(0)}. \quad (20)$$

The suppression factor α is on the order of 0.005. The use of such a small value for α maintains the stability in numerical iterations. Using the new value for $D_e^{(1)}$, we repeat the above removal-retrieval procedures to obtain $D_e^{(2)}$. The iteration process is carried out until $D_e^{(n)}$ satisfies the following convergence criterion:

$$\frac{|D_e^{(n)} - D_e^{(n-1)}|}{D_e^{(n-1)}} < 1.0 \times 10^{-4}. \quad (21)$$

3. SENSITIVITY STUDIES AND ERROR ANALYSES

Sensitivity studies have been performed using the midlatitude summer atmospheric profile. First, we must generate simulated thermal infrared and solar clear and cloudy radiances. Spectral transmittances for the 3.7 μm and 10.9 μm wavelengths have been computed by using the program developed by Weinreb and Hill (1980), in which the instrument filter function is accounted for. The simulated upwelling IR radiances for clear sky are computed using the solution of the basic radiative transfer equation in the forms

$$R_{a3ir} = B_3(T_s)T_3(p_s) + \int_0^{p_s} B_3(T) \frac{\partial T_3(p)}{\partial p} dp, \quad (22a)$$

$$R_{a4} = B_4(T_s)T_4(p_s) + \int_0^{p_s} B_4(T) \frac{\partial T_4(p)}{\partial p} dp, \quad (22b)$$

where p_s and T_s are the surface pressure and temperature, respectively, and $T_i(p)$ are the atmospheric transmittances at pressure level p . In the simulations, cloud-base heights are prescribed at 7, 9, and 11 km. The cloud temperatures and mean ice crystal sizes can be determined from the temperature profile. For each cloud-base height, calculations are carried out for 10 optical depths (0.125, 0.25, 0.5, 1.0, 2.0, 4.0, 8.0, 16.0, 32.0, 64.0). Emissivity values are obtained from Eq. (13). The upwelling thermal infrared cloudy radiances are then computed from Eq. (12).

To compute the Ch. 3 solar radiance for clear and cloudy skies, we first set the effective surface albedos for Chs. 1 and 3 to be 0.12 and 0.1, respectively. The geometric parameters used are: solar zenith angle, $\theta_0 = 71^\circ$; satellite zenith angle, $\theta = 40^\circ$; and relative azimuthal angle, $\Delta\phi = 146^\circ$. This set is based on the geometric parameters involving the FIRE-I-IFO data. The clear solar radiance for Ch. 3 is computed as follows:

$$R_{a3sol} = \mu_0 F_{03} r_{a3}, \quad (23)$$

while the cloudy solar radiance for Ch. 3 is computed from Eq. (18). It follows that the simulated Ch. 3 radiances for both cloudy and clear atmospheres are given by

$$R_3 = R_{3ir} + R_{3sol}, \quad (24)$$

$$R_{a3} = R_{a3ir} + R_{a3sol}. \quad (25)$$

Figure 4(a) and 4(b) show the distributions of R_{3ir} and R_3 ($= R_{3sol} + R_{3ir}$) versus R_4 , respectively, for the three cloud heights and 10 optical depths. In each plot, the Planck intensity curve is included as a reference. The curves of constant cloud height are all above the Planck intensity curve. The uppermost point where all the curves converge represents clear radiances. The lowest point for each curve corresponds to the highest optical depth. The curvature of the curves in Figure 4(b) is due to the variation in R_{3sol} . By comparing Figures 4(a) and 4(b), we note that R_3 is larger than R_{3ir} by about $0.05\text{--}0.2 \text{ mW/m}^2/\text{sr/cm}^{-1}$ due to additional solar reflections for the present sun-satellite geometry. This difference will increase as the sun becomes closer to the zenith. Moreover, in Figure 4(a), when the emissivity approaches 1 for the largest optical depth, both R_{3ir} and R_4 approach $B_3(T_c)$ and $B_4(T_c)$, respectively. However, in Figure 4(b), the total Ch. 3 radiance $R_3 > B_3(T_c)$. The difference between R_3 and $B_3(T_c)$ is mainly due to the size effect on the solar component as well as the atmospheric absorption and surface reflection.

Figure 5 illustrates the ratio of R_{3sol} to R_{3ir} as a function of τ and cloud-base height. Variation in the relative magnitude of R_{3sol} and R_{3ir} can be seen. For the present sun-satellite geometry, this ratio increases with τ . For thin cirrus ($\tau < 1$), R_{3ir} is 10 times larger than R_{3sol} and is almost independent of cloud height. However, for thick cirrus, R_{3sol}/R_{3ir} approach asymptotic values,

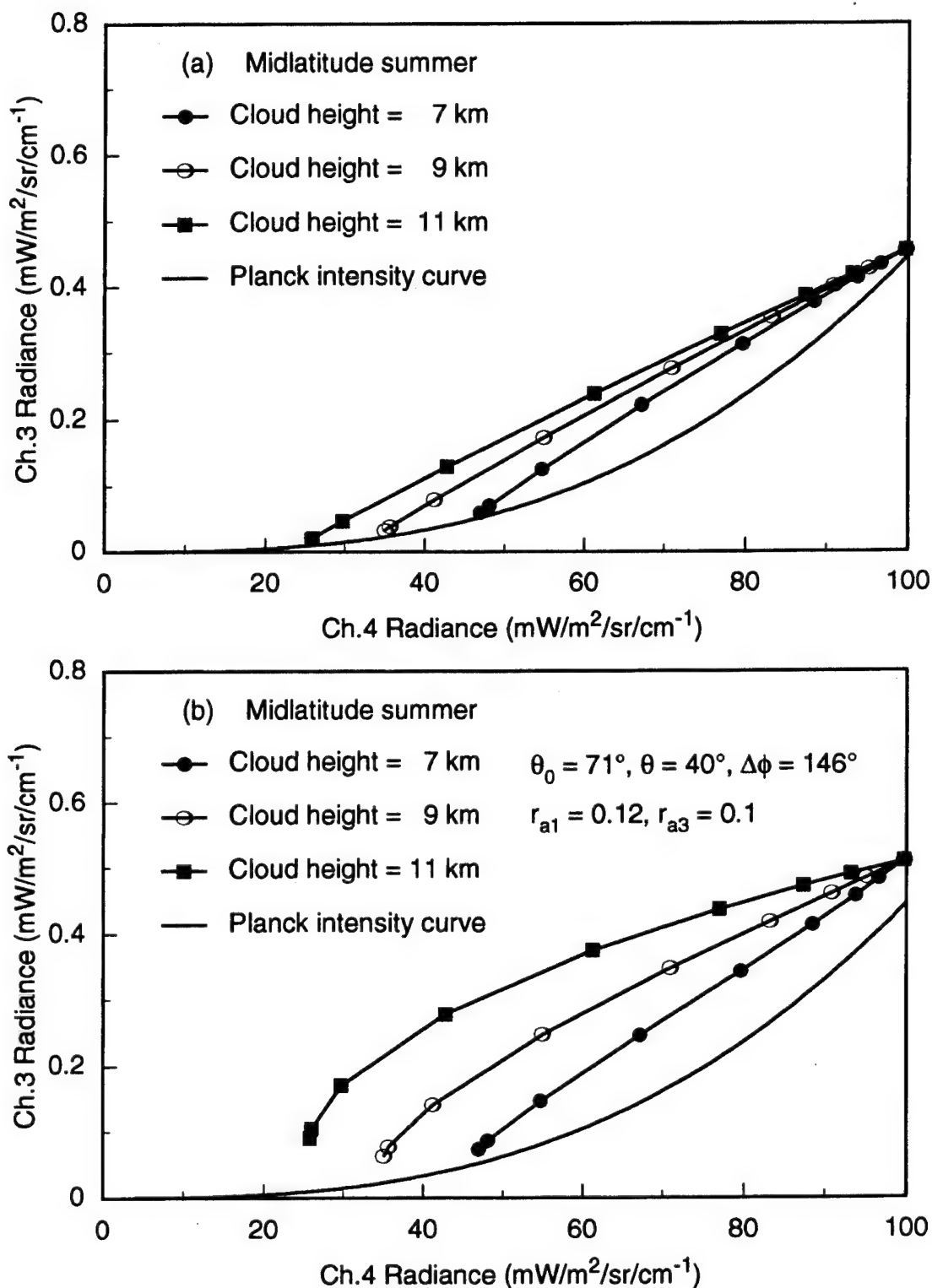


Fig 4. (a) Distribution of the simulated Ch. 3 thermal infrared (R_{3ir}) and Ch. 4 (R_4) radiances for three cloud heights. Also depicted in the figure is the Planck intensity curve. (b) Distribution of the simulated Ch. 3 solar plus thermal infrared (R_3) and Ch. 4 (R_4) radiances for the same three cloud heights.

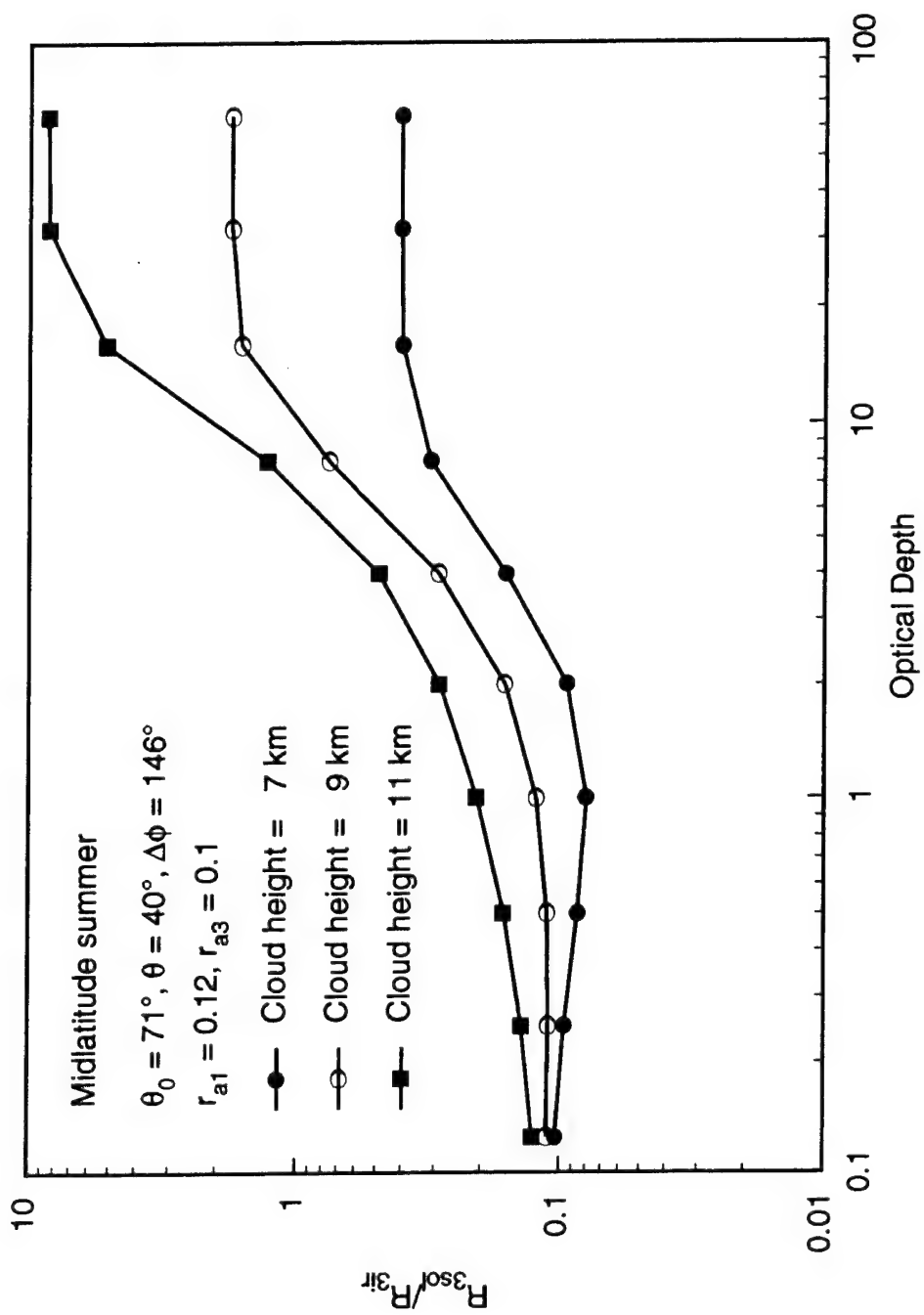


Fig 5. The ratio of the Ch. 3 solar (P_{3sol}) to IR (P_{3ir}) components as a function of the optical depth for three cloud heights.

because R_{3ir} approaches the Planck intensity value at the cirrus cloud temperature. R_{3sol} also approaches its asymptotic value. Moreover, the radiance ratio increases with the cloud-base height, because of the coupling of lower cloud temperatures and smaller ice crystals. The former leads to smaller R_{3ir} values, while the latter produces stronger solar reflection. For the present sun-satellite geometry, Figure 5 shows that the Ch. 3 solar component is at least 10% of the total radiance which can not be ignored.

In the following, we investigate the effects of uncertainties in the input parameters on the accuracy of the removed solar component. Errors in the $3.7 \mu m$ solar component can be due to uncertainties in the mean effective size (D_e), as well as the Chs. 1 and 3 effective surface albedos (r_{a1} and r_{a3}).

First, the effects of uncertainties in D_e on the accuracy of the Ch. 3 solar radiance (R_{3sol}) are studied. From the three prescribed cloud-base heights of 7, 9, and 11 km, mean D_e values of 136, 81, and $52 \mu m$ are obtained. Next, R_{3sol} and the total Ch. 3 radiance (R_3) are computed for each D_e value, as well as for a number of optical depths. We assume that r_{a1} and r_{a3} are the exact values and that the value of D_e used in the scheme has a range of uncertainty, $\Delta D_e = \pm 5 \mu m$. We then proceed to quantify R_{3sol} by using the look-up table, as displayed in Figure 3. Errors in R_{3sol} will result due to the uncertainty in D_e . Figure 6(a) shows the maximum percentage errors for $\Delta R_{3sol}/R_{3sol}$ as functions of optical depth. The relative error $\Delta R_{3sol}/R_{3sol}$ increases with the optical depth. For small optical depths, ΔR_{3sol} is small because R_{3sol} is dominated by surface reflection. For thicker clouds, the reflected radiances are dominated by cloud reflection and the effects of ΔD_e become important. Since R_{3sol} approaches an asymptotic value for $R_1 > 0.4$ (Figure 3) and since the range of ΔD_e is fixed at $\pm 5 \mu m$, $\Delta R_{3sol}/R_{3sol}$ also approaches an asymptotic value. The error in $\Delta R_{3sol}/R_{3sol}$ for the 7-km cloud case is smaller than the errors for the 9- and 11-km cloud cases, because the former has a D_e larger than $100 \mu m$. Note that R_{3sol} is

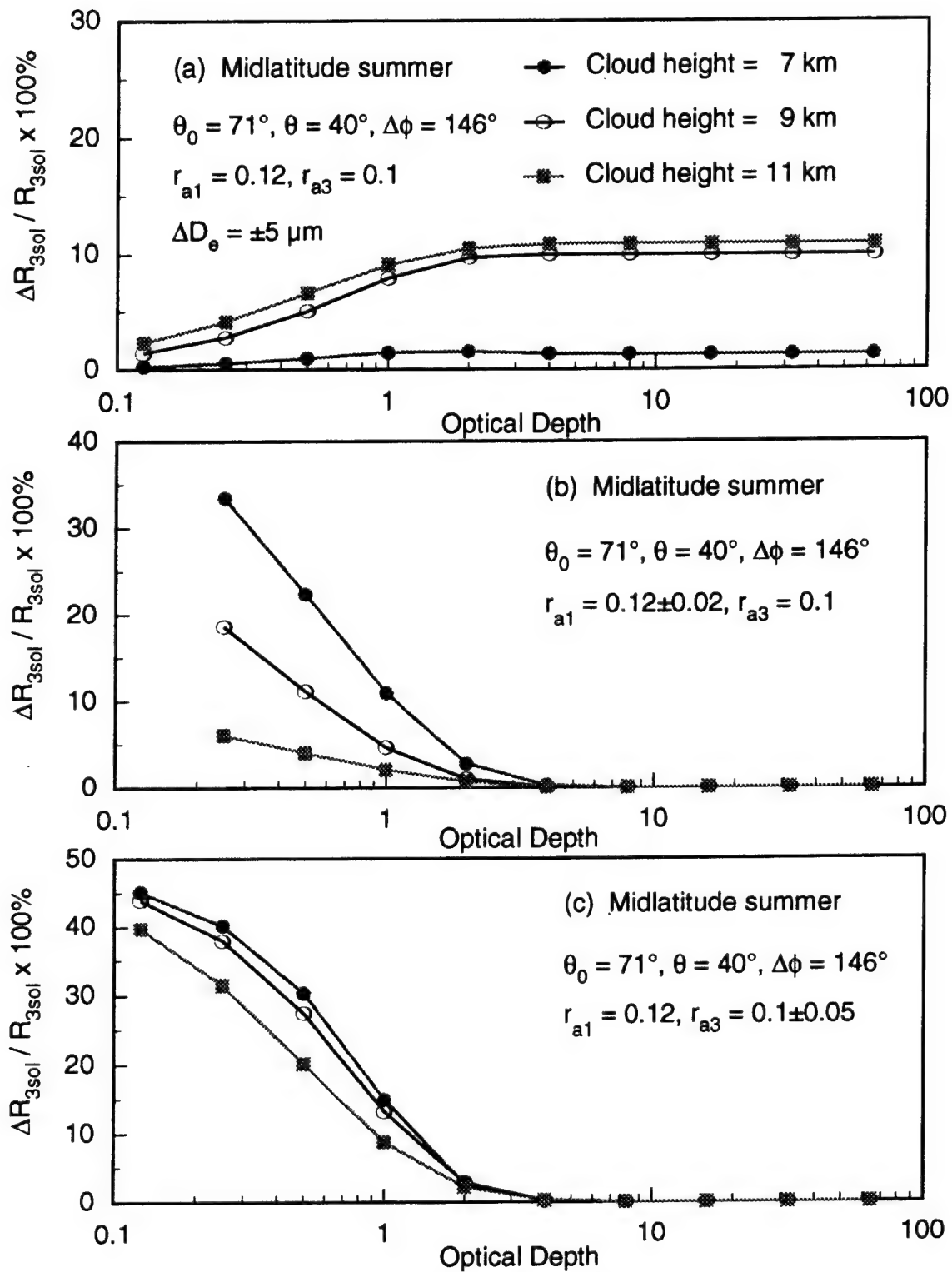


Fig 6. Maximum percentage errors in the Ch. 3 solar radiance (R_{3sol}) produced by the errors in (a) the mean effective size, ΔD_e , of $\pm 5 \mu\text{m}$, (b) the Ch. 1 mean effective surface albedo, Δr_{a1} , of ± 0.02 , (c) the Ch. 3 mean effective surface albedo, Δr_{a3} , of ± 0.05 .

nearly constant for $D_e > 100 \mu\text{m}$ (Figure 3). Overall, the maximum error of $\Delta R_{3\text{sol}}/R_{3\text{sol}}$ is less than 12%.

Next, we investigate the effects of uncertainties in r_{a1} on the accuracy of $R_{3\text{sol}}$. We assume that D_e and r_{a3} are both known without errors, but r_{a1} has an uncertainty of ± 0.02 . Errors in $R_{3\text{sol}}$ will be produced due to the uncertainty in r_{a1} . Figure 6(b) shows the maximum percentage errors in $R_{3\text{sol}}$ as functions of optical depth. In contrast to Figure 6(a), $\Delta R_{3\text{sol}}/R_{3\text{sol}}$ decreases as the optical depth increases. This decrease occurs because the reflected radiances are essentially controlled by cloud reflection for larger optical depths, so that the changes in the effective surface albedo have little effect. For smaller optical depths, $\Delta R_{3\text{sol}}/R_{3\text{sol}}$ is larger for the 7-km cloud than for the 9- and 11-km clouds, because $R_{3\text{sol}}$ is much smaller for larger D_e s associated with the 7-km cloud. Overall, for optical depths larger than 1, the maximum $\Delta R_{3\text{sol}}/R_{3\text{sol}}$ is less than 12%.

We also investigate the effects of uncertainties in r_{a3} on the accuracy of $R_{3\text{sol}}$. It is assumed that D_e and r_{a1} values are exact. However, r_{a3} has an uncertainty of ± 0.05 , which will result in errors in $R_{3\text{sol}}$. Figure 6(c) shows the maximum percentage errors in $R_{3\text{sol}}$ as functions of optical depth. As in Figure 6(b), $\Delta R_{3\text{sol}}/R_{3\text{sol}}$ decreases as the optical depth increases. In addition, for smaller optical depths, $\Delta R_{3\text{sol}}/R_{3\text{sol}}$ is smaller for the 11-km cloud, because the value of $R_{3\text{sol}}$ is larger for smaller D_e associated with higher clouds. For optical depths larger than 1, the maximum $\Delta R_{3\text{sol}}/R_{3\text{sol}}$ is less than 15%.

Errors in the retrieved cirrus parameters can be due to instrument noises and the errors in r_{a1} and r_{a3} . To perform error analyses, the probability of the error produced by a particular parameter χ , $\Delta\chi$, is assumed to follow the Gaussian distribution in the form:

$$p(\Delta\chi) = \frac{1}{\sigma\sqrt{2\pi}} \exp[-(\Delta\chi^2/2\sigma^2)], \quad (26)$$

where σ is the standard deviation. The Gaussian distribution differs from random distribution in that the latter would give a uniform probability of error within the prescribed error bounds, while the former would give a decreasing probability of error as the error increases. The Gaussian distribution appears to be more representative of a realistic error distribution than the random distribution. We have used an established software as the Gaussian distribution generator to simulate various error distributions with the following specified standard deviations: for the Ch. 3 noise, $\sigma = 0.4$ K; for the Ch. 4 noise, $\sigma = 0.12$ K; for the Ch. 1 effective surface albedo, $\sigma = 0.02$; and for the Ch. 3 effective surface albedo, $\sigma = 0.05$. The σ values for Ch. 3 and Ch. 4 noises are prescribed based on the values described by Dudhia (1989). The σ value for the Ch. 1 surface albedo is based on the realistic histogram for Ch. 1 reflectances. The σ value for the Ch. 3 mean effective surface albedo is based on the range of laboratory measurements (Sutherland, 1986) for $3.7 \mu\text{m}$ surface reflectances.

To carry out the error analysis, we generate three thousand sets of errors in both instrument noises and the prescribed parameters. Figures 7 (a)-(d) show, respectively, the root-mean-square (rms) errors for the Ch. 3 solar component, the cirrus cloud temperature, the mean effective size, and the optical depth, as functions of the prescribed optical depth for three cloud-base heights. In all cases, rms errors decrease with increasing optical depths because the effects of the uncertainty in effective surface albedo on cloudy radiances become less as the optical depth increases. Moreover, for thin cirrus clouds, slight perturbations in both radiances due to instrument noises would lead to large errors in the retrieved parameters. For optical depths larger than 8, the percentage error in the optical depth increases [Figure 7(d)] because the emissivity approaches 1 and a slight error in it would lead to a large error in

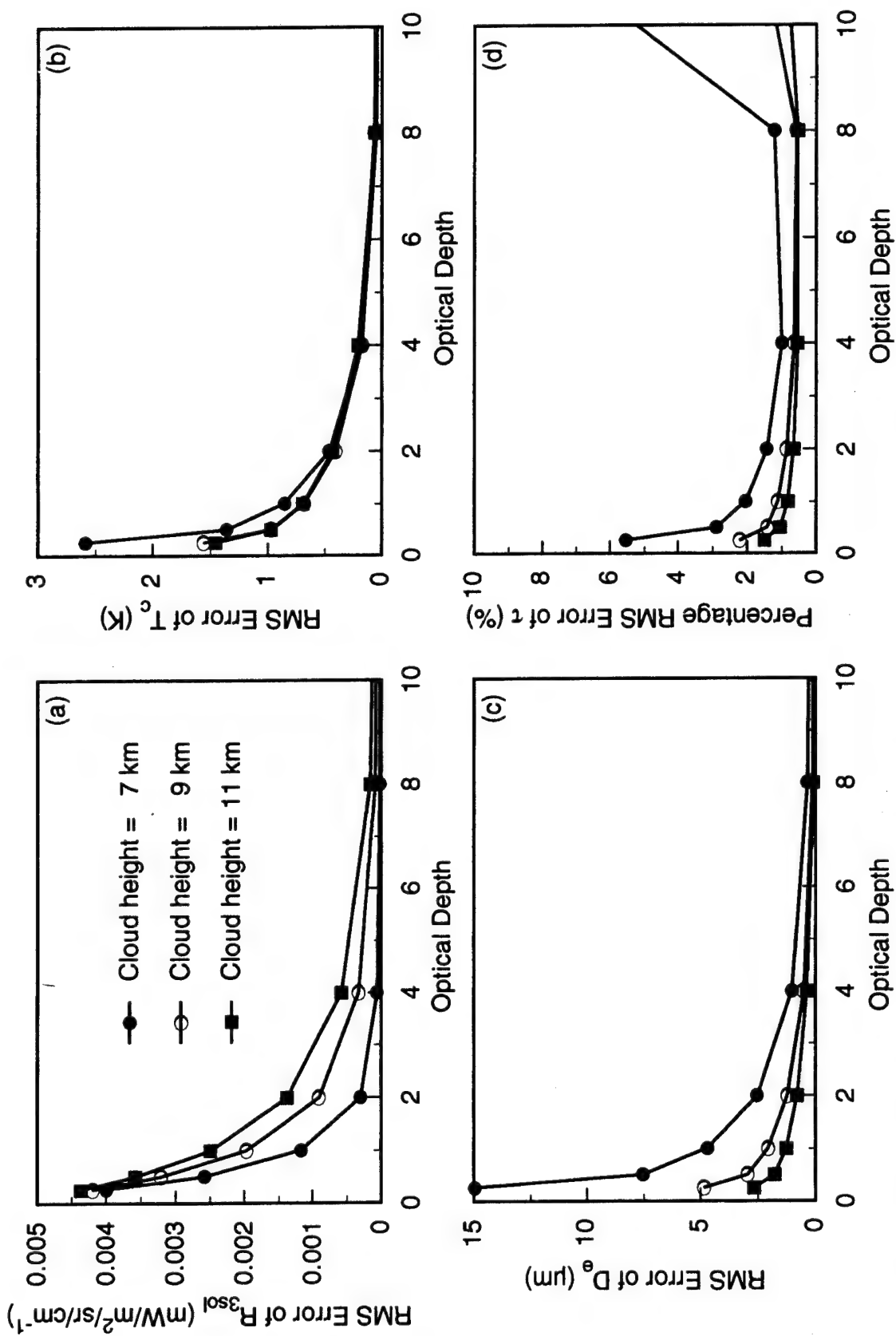


Fig 7. Root-mean-square (rms) errors in (a) the Ch. 3 solar component (b) cirrus cloud temperature, (c) mean effective size, and (d) optical depth produced by Ch. 3 noise ($\sigma = 0.4$ K), Ch. 4 noise ($\sigma = 0.12$ K), uncertainties in Ch. 1 surface albedo ($\sigma = 0.02$), and uncertainties in Ch. 3 surface albedo ($\sigma = 0.05$) as functions of the optical depth.

the optical depth. For optical depths greater than 0.25, the rms errors in R_{3sol} , T_c , D_e , and τ , are less than 0.0045 mW/m²/sr/cm⁻¹ (or 5%), 2.6 K, 15 μ m, and 6%, respectively, indicating that the removal-retrieval scheme is numerically stable and the retrieval accuracy is acceptable. The rms errors in T_c are of the same order of magnitude as the rms differences between the retrieved and lidar derived values (Table 3, Minnis et al., 1993b). Moreover, the rms errors in D_e are less than the uncertainty in the D_e determined from the aircraft measurements (Heymsfield and Platt, 1984).

The retrieval accuracy depends on the cloud height and varies for the retrieved cloud parameters. Errors in R_{3sol} increase with decreasing cloud height. Errors in T_c are virtually independent of cloud height for optical depths greater than 2. However, for optical depths smaller than 2, errors increase with decreasing cloud height. This behavior is related to errors in D_e , which increase with decreasing cloud height, as shown in Figure 7(c). In the retrieval scheme, the parameters D_e , k_4/k_3 , and T_c and the associated errors are interrelated through Eqs. (15) and (17). Moreover, when the cloud is lower, cloud temperature is higher, while ice crystal size is larger and k_4/k_3 approaches its asymptotic values in the case of lower clouds. A small error in k_4/k_3 would lead to large errors in both D_e and T_c . Finally, in Figure 7(d), errors in the optical depth are shown to increase with decreasing cloud height. This implies that errors in the related cloud emissivity increase with cloud temperature.

Effects of other uncertainties on the accuracy of the removal-retrieval scheme are discussed in the following. Based on Figure 3, errors in the Ch. 1 radiance do not affect significantly on the accuracy of the removed solar component for optical depths larger than one, because the Ch. 3 radiance is close to the asymptotic value. For optical depths smaller than 1, errors of the removed solar component depend on the effective surface albedo for both channels

and the ice crystal sizes. The inhomogeneity of cirrus clouds would have an important effect on their radiative properties. However, it is not feasible to retrieve the detailed structure of clouds utilizing the infrared methodology. The retrieval results would represent the averaged cloud characteristics over the AVHRR pixels. It appears to us that the effects of ice crystal shape and cloud inhomogeneity on the radiative properties of clouds will require considerable research before their impacts on satellite remote sensing can be understood. Finally, regarding the effects of errors in the polynomial fitting of k_4/k_3 vs. D_e , we have shown that the root-mean-square difference between the computed and least-squares fitted values of k_4/k_3 is 0.045, revealing that the polynomial fitting is an excellent parameterization to relate k_4/k_3 and the mean effective size (Ou et al., 1993). Thus, it is not necessary to study on the sensitivity of errors in the parameterization of k_4/k_3 on the retrieval.

4. APPLICATION OF SATELLITE DATA ASSOCIATED WITH FIRE-I-IFO

For the purpose of testing the removal-retrieval scheme, we have acquired the AVHRR Global Area Coverage (GAC) data collected by NOAA 9 at about 2100 UTC, 28 October 1986. This data set, including the FIRE-I-IFO region (42° - 47° N; 87° - 92° W), covers the midwestern United States. It contains the scaled values of latitude, longitude, solar zenith angle, the zenith-normalized Chs. 1 and 2 radiances, and the brightness temperatures of Chs. 3, 4, and 5 for each GAC pixel. There are a total of 2.6×10^5 pixels. A program has been developed to unpack the data set, using the calibration procedures documented by Kidwell (1991) to obtain the true data values. We have also developed a program to compute the satellite zenith angle and the relative azimuthal angle based on the viewing geometry of the polar-orbiting satellite. The thermal infrared channels (3, 4, and 5) are constantly calibrated by blackbody calibrators on board the satellite. However, there are no in-flight calibration facilities to monitor the long-term stability of visible channels (1 and 2). Staylor (1990) has estimated that the rate of degradation for these visible channels is about 6% per year. We have accounted for these effects in the calibration procedures.

Using the foregoing data, we have performed retrievals of cirrus cloud parameters over three areas with different scales, as shown in Figure 8. We first apply the removal-retrieval scheme to a $1^{\circ} \times 1^{\circ}$ area over western Wisconsin (the innermost frame in Figure 8). We then expand the domain of retrievals to a $5^{\circ} \times 5^{\circ}$ area associated with the FIRE-I-IFO region (the intermediate frame in Figure 8). These retrievals are designed for developing and testing an automated removal-retrieval scheme, for verifying the retrieval results against local lidar measurements, and for comparing the retrieval results with those determined from different satellite data sets and retrieval methodologies. The third retrieval domain is the $20^{\circ} \times 30^{\circ}$ area over the midwestern United States. These retrievals enable us to test the removal-retrieval scheme over a large area with different

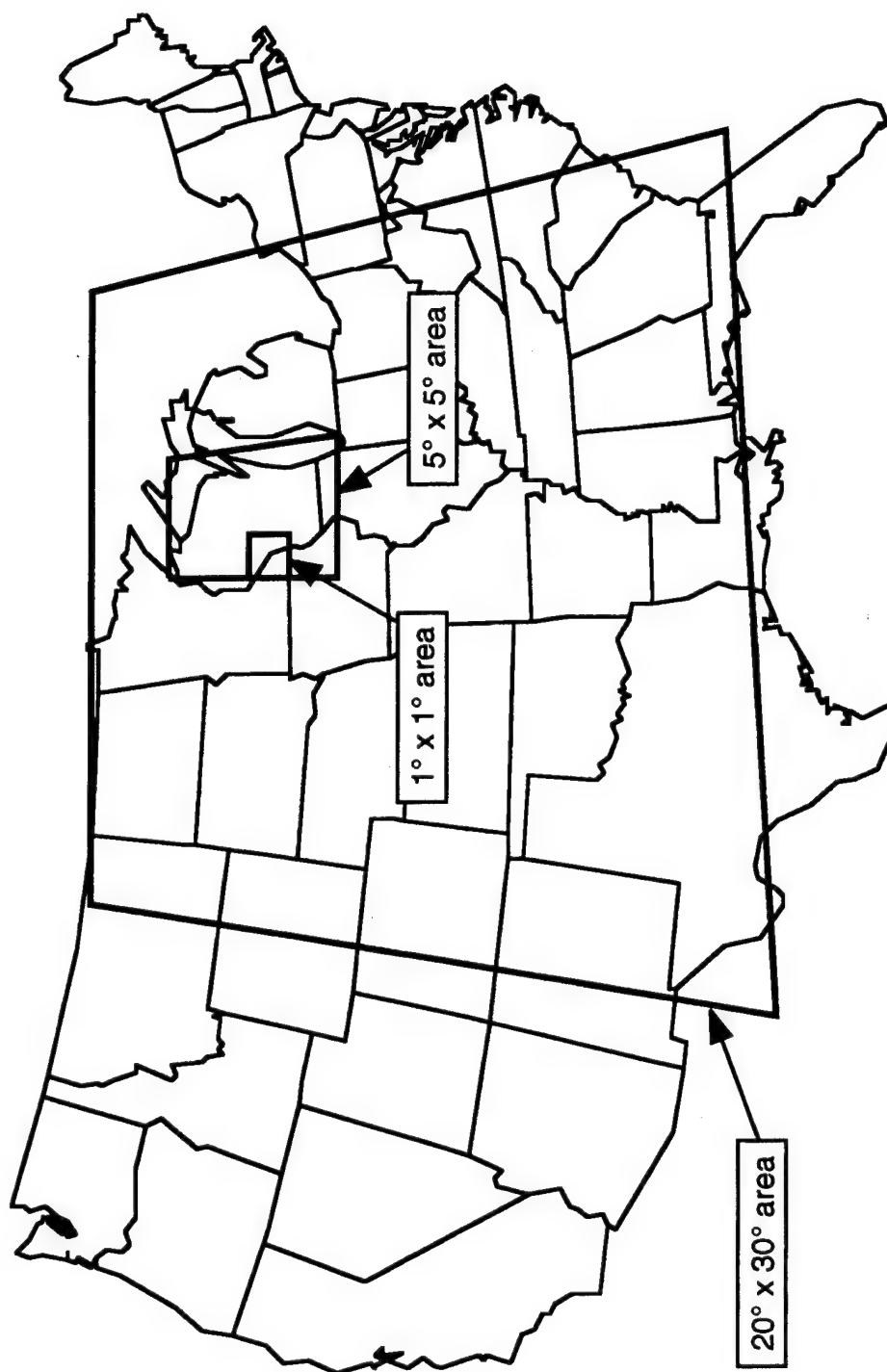


Fig 8. Three different domains for daytime retrievals over the United States. The smallest one is a $1^\circ \times 1^\circ$ zone over western Wisconsin. The intermediate one is $5^\circ \times 5^\circ$ area over Wisconsin. The largest one is a $20^\circ \times 30^\circ$ region covering the midwestern United States.

satellite viewing geometries and surface characteristics. We also compare our retrieval results with the AVHRR visible cloud picture for the same time period and area.

4.1 Retrievals over a $1^\circ \times 1^\circ$ Area

We have tested the removal-retrieval scheme over a small area ($1^\circ \times 1^\circ$) west of Fort McCoy. Results of this test are presented in the following. The selected zone extends from 43.5° to 44.5°N and from 91° to 92°W . Within this area, there are 392 GAC pixels. Figures 9(a)-(c) show the halftone display of the Ch. 1 reflectances and the Ch. 3 and Ch. 4 brightness temperatures. The darker areas in each frame correspond to lower reflectances or higher brightness temperatures, and are associated with either clear or very thin cirrus clouds. The whiter areas correspond to higher reflectances or lower brightness temperatures, and are associated with thicker cirrus clouds. The area is mostly covered with clouds during the day. Small clear areas are evident over the eastern and southwestern regions. High reflectances and low brightness temperatures preside over the south-central region. Brightness temperatures are distributed more evenly over the northern half of the area than those over the southern half. This suggests that at the time of satellite overpass, the air mass over the southern half was more dynamically active than the northern half. The clear detection scheme is applied to the satellite data covering the aforementioned area. Figure 10 shows the distribution of clear (\bullet) and cloudy (\diamond) pixels. There are 46 detected clear pixels, which are scattered over the eastern and southwestern regions. The clear areas shown in Figure 9(a) and 9(b) are correctly identified in Figure 10.

To remove the $3.7 \mu\text{m}$ solar component, we must first determine r_{a1} and r_{a3} . The Ch. 1 effective surface albedo (~ 0.12) is taken to be the mode value of r_1 for all the identified clear pixels. The determination of r_{a3} is somewhat more involved. As described earlier, the surface albedo r_{s3} is fixed at 0.1.

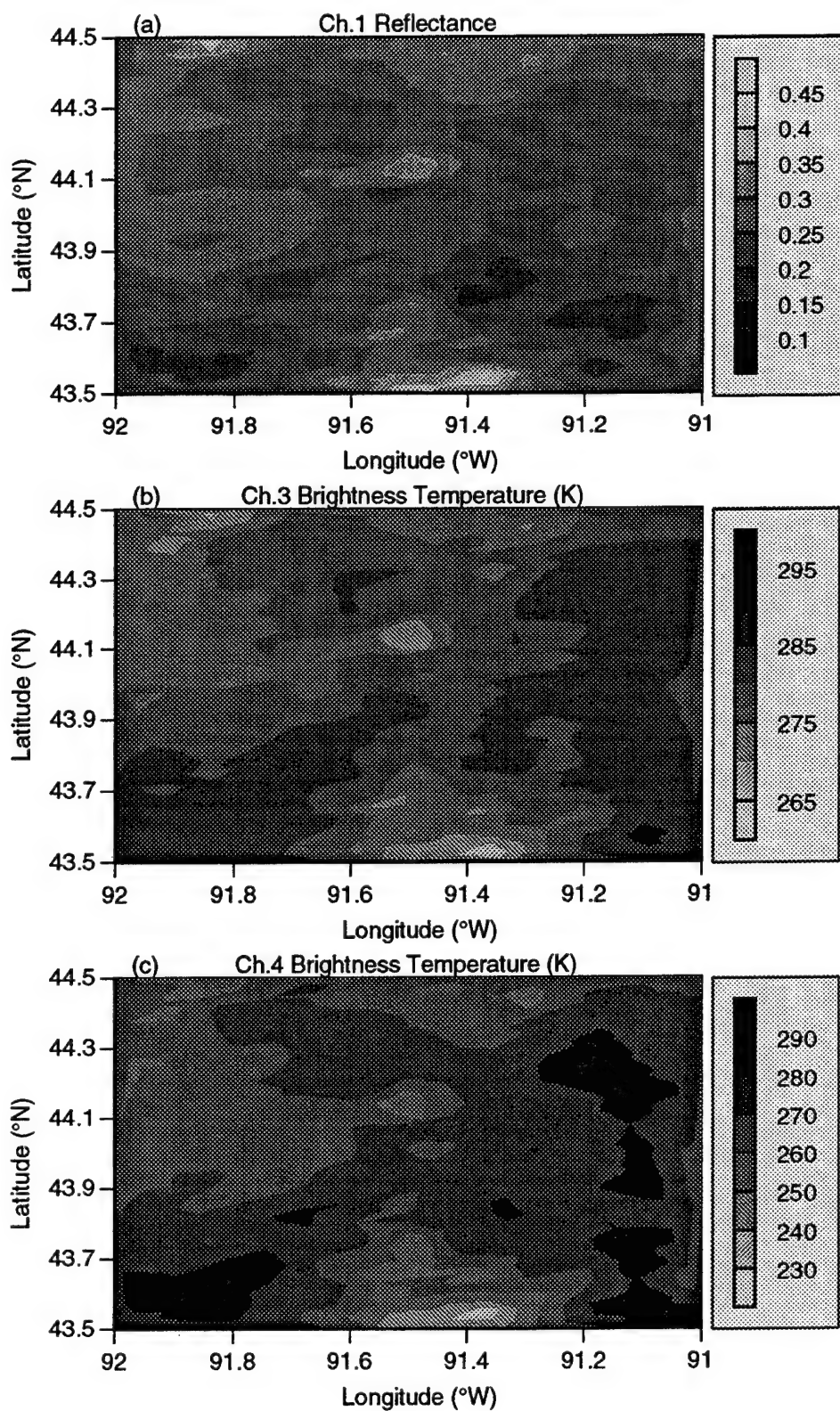


Fig 9. Half-tone display of (a) the Ch. 1 reflectance, (b) the Ch. 3 brightness temperature, and (c) the Ch. 4 brightness temperature, for the $1^\circ \times 1^\circ$ area ($43.5^\circ - 44.5^\circ\text{N}$, $91^\circ - 92^\circ\text{W}$) over Wisconsin at 2100 UTC, 28 October 1986.

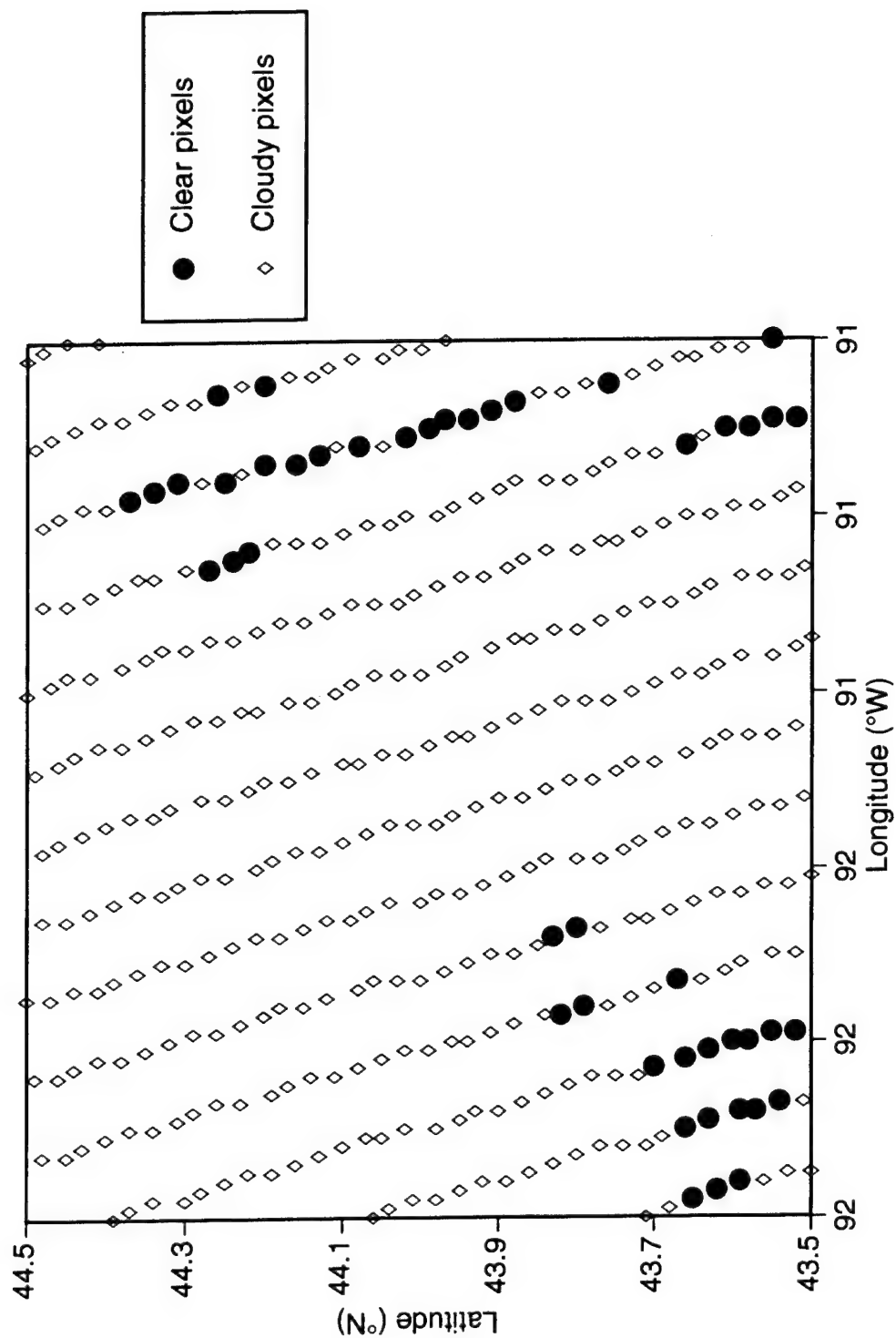


Fig 10. Distribution of the clear and cloudy pixels that are identified over the $1^{\circ} \times 1^{\circ}$ area west of Fort McCoy.

However, to determine r_{a3} from Eq. (6), the value of T_3 is required. Two sets of sounding data over the region at 2100 UTC are used in the T_3 calculations. One set is the Green Bay sounding presented by Starr and Wylie (1990), while the other is derived from the ISCCP-C1 sounding profiles (Rossow and Schiffer, 1991). The ISCCP sounding profiles are the averages of satellite-derived sounding profiles over a $2.5^\circ \times 2.5^\circ$ area at nine vertical levels. Generally, the temperatures of these two profiles differ by less than 10 K, while the humidities differ by less than 2g/kg above 700mb. The transmittance profiles for the $3.7 \mu\text{m}$ wavelength are computed using the two sets of soundings. The total transmittance in both cases is about 0.99 because of the low humidity content, implying that the simulated Ch. 3 transmittance is relatively insensitive to the uncertainty in sounding profiles.

We apply the removal-retrieval scheme to each cloudy pixel that has been identified. As investigated in Ou et al. (1993), the cirrus cloudy condition can be found as the brightness temperature difference between Ch. 3 (nighttime) and Ch. 4 larger than 2K. The Ch. 3 daytime data, which is contaminated by the solar reflection, cannot be used to identify the presence of cirrus. However, cirrus pixels can be detected from the retrieved cloud temperature. Figures 11(a)-(c) show the halftone displays of the retrieved T_c , D_e , and τ over the $1^\circ \times 1^\circ$ area, respectively. The distribution of T_c over the northwestern region is relatively homogeneous with values between 230 and 240 K. Sharp-transition regions are evident near cold cirrus clouds ($T_c < 225$ K). These features result from the presence of cold cirrus within a clear region. The cold cirrus clouds appear to be associated with cirrus generation regions (Heymsfield, 1975). These clouds are relatively high and thin and contain small ice crystals [see Figure 11(b) and (c)].

From the distribution of cirrus cloud temperature, we may also qualitatively infer the dynamic activity of the air mass. To the north and east

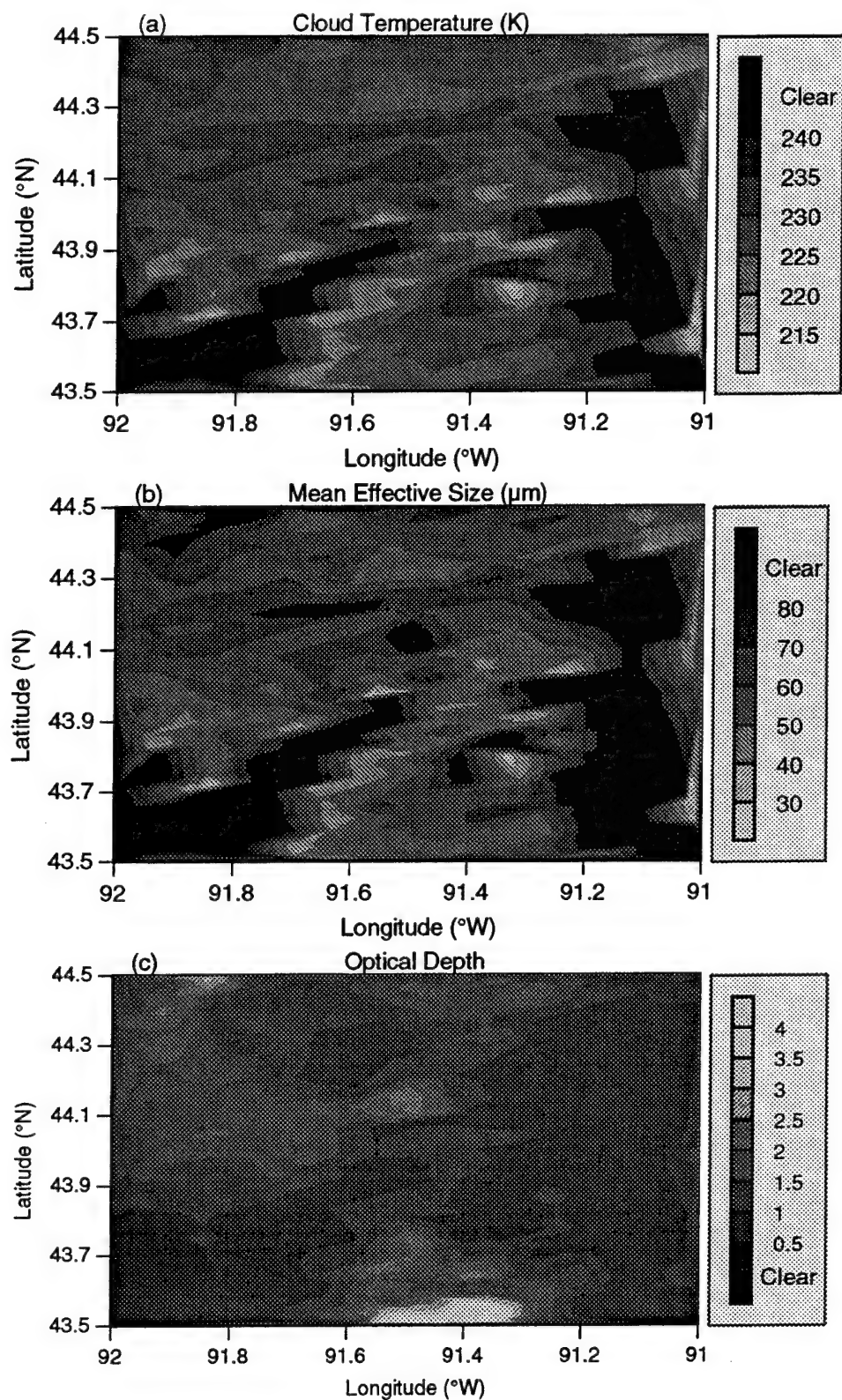


Fig 11. Half-tone display of the (a) retrieved cloud temperature, (b) the retrieved mean effective size, and (c) the retrieved optical depth, over the 1° x 1° area west of Fort Mcloy at 2100 UTC, 28 October 1986.

of the sharp-transition regions, the distribution of cirrus cloud temperatures is less variant. A transition is seen from the cirrus growing regions, located at the southwestern side of the cloudy area, to the cirrus dissipating regions, located at the northeastern side. Considering that the prevalent wind is from the west-south-west direction (Starr and Wylie, 1990), this transition pattern may be explained by the theory of cirrus formation-dissipation proposed by Heymsfield (1975). The stable regions over the northern part show that the cirrus clouds there are dissipating. We conclude that the cirrus growing regions on the southwestern side are dynamically active with vertical motions enhanced by latent heat release, whereas the cirrus dissipating regions on the northeastern side are dynamically stable. It is likely that within a small area on the order of $100 \times 100 \text{ km}^2$, newly formed cirrus coexists with mature and dissipating cirrus.

In Figure 11(b), the distribution of D_e corresponds to the distribution of T_c . Sharp-transition regions occur over the southern and eastern parts of the area. Over the northern part, the distribution of D_e is relatively uniform, the distribution of τ , shown in Figure 11(c), is also relatively uniform ($\tau = 0 - 2.5$), except near the south-central part, where τ reaches a value greater than 5. It is noted that the distribution of τ does not necessarily match the distribution of T_c . Most of the cold cirrus and warm cirrus regions show relatively small values of τ ($0 \sim 1.5$). Thick cirrus clouds occurring over the south-central part represent a region with high ice water path.

4.2 Retrievals over a $5^\circ \times 5^\circ$ Area

We have also applied the removal-retrieval scheme to the AVHRR daytime data, collected on 28 October 1986 at 2100 UTC over Wisconsin (42° to 47°N ; 87°W to 92°W) during the FIRE-I-IFO. The brightness temperature of Ch. 4 over this area is shown in Figure 12. The majority of the cloudy areas is located near the northwest corner, at about 44°N and 91°W and 45°N and 89°W . These areas are all

characterized by brightness temperatures lower than 260 K. Clear areas are located mainly at 45°N and 90°W and near the northeast and southeast corners.

To reduce the effects of surface inhomogeneity on the mean clear radiances, the whole 5° x 5° area is divided into 25 1° x 1° boxes to which the clear/cloud detection scheme is applied. Using the brightness temperatures of clear pixels that are identified, we compute a pair of Ch. 3 and Ch. 4 thermal infrared mean clear radiances for each box. Because of the required criteria for detecting clear pixels, some boxes contain no identifiable clear pixels. In these cases, the mean clear radiances of a neighboring box are used. The removal-retrieval scheme is then applied to each box.

Figures 13(a)-(d) show the geographic distribution of the retrieved cloud temperature, mean effective ice crystal size, optical depth, and cloud height over the 5° x 5° area, respectively. In Figure 13(a), the retrieved cloud temperatures range between 215 and 240 K. The distribution of the retrieved cloud temperature is different from that of the Ch. 4 brightness temperatures. For example, near the northwest corner, where the Ch. 4 brightness temperatures are about 240 K, the minimum cloud temperature is about 225 K. Around 45°N and 89°W, the Ch. 4 brightness temperatures are also about 240 K, while the cloud temperatures are about 235 K. However, one degree longitude east of this cloudy area, the Ch. 4 brightness temperatures are about 255 K, while the minimum cloud temperature is about 220 K. It is possible that cirrus clouds are on top of low clouds near 45°N and 89°W. However, a single layer of high, thin cirrus clouds is present near 45°N and 88°W. Over the region where multi-layered clouds are present, retrievals had been performed as though there were only a single layer of cloud. This is because reliable methods are yet to be developed for detecting multi-layer cloudy pixels using AVHRR data. In Figure 13(b), the distribution of the retrieved mean effective ice crystal sizes, which range between 40 and 100 μm , are in agreement with that of the cloud temperature shown in Figure 13(a).

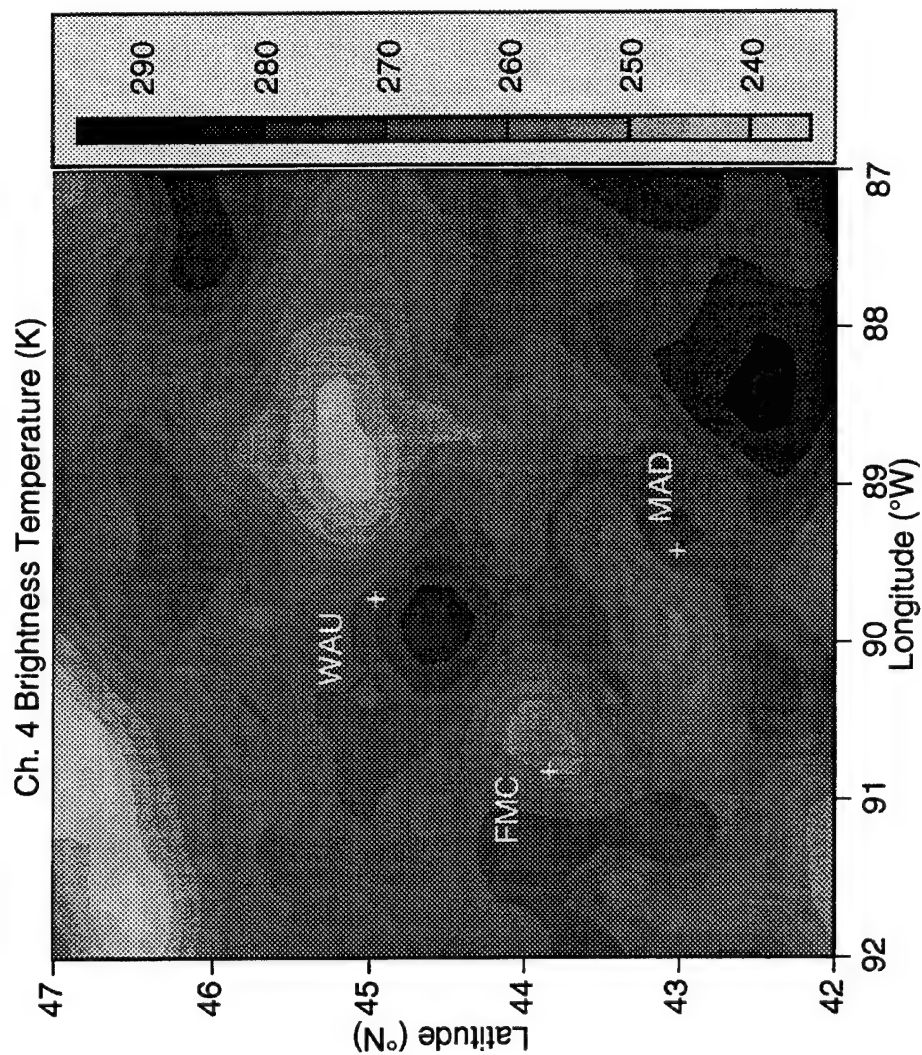


Fig 12. Half - tone display of the Ch. 4 brightness temperature for the 5° x 5° area over Wisconsin at 2100 UTC, 28 October 1986. The symbols "+" identify the location of three FIRE-I-IFO stations (see text).

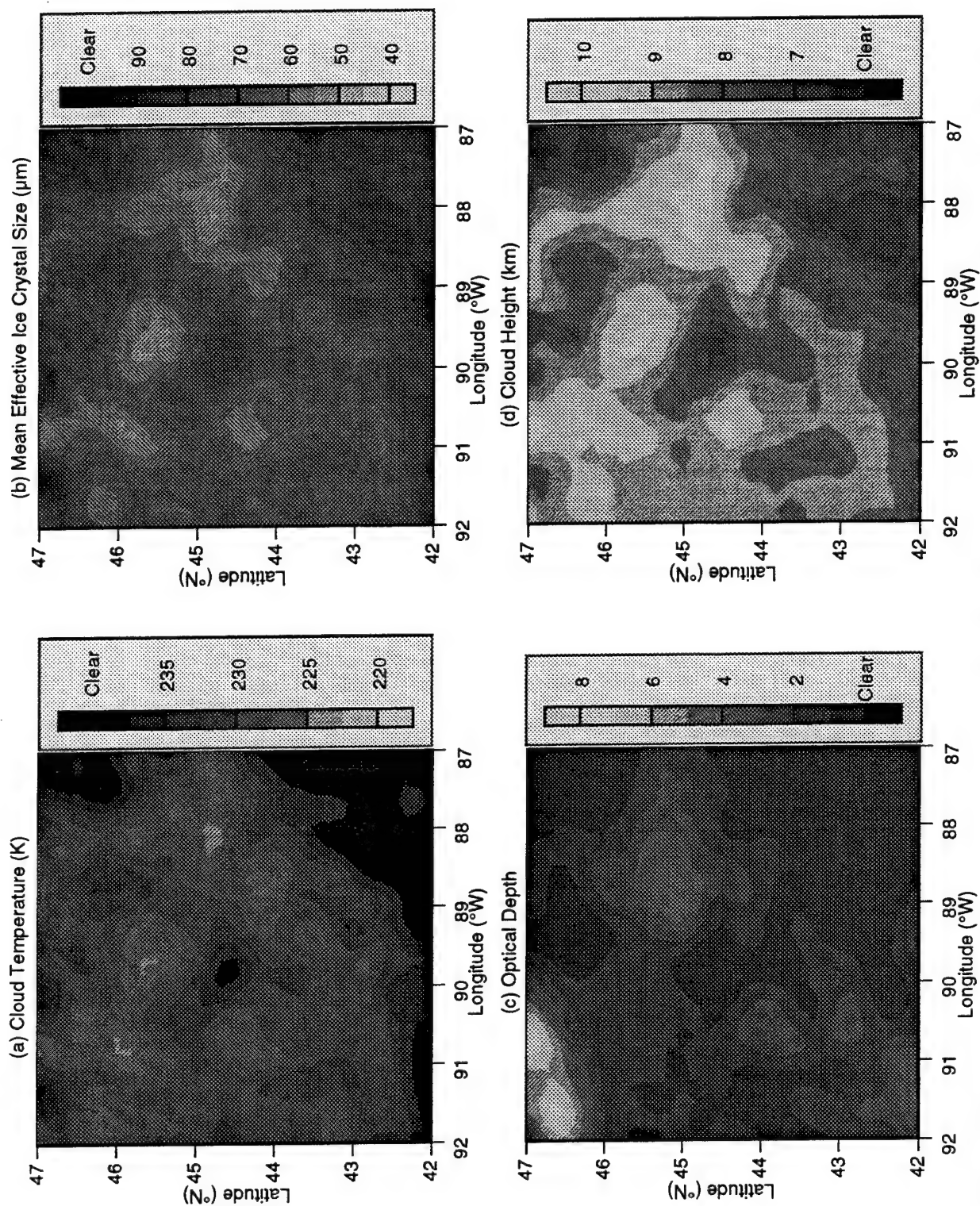


Fig 13. Half - tone display of the (a) retrieved cloud temperature, (b) the retrieved mean effective size, (c) the retrieved optical depth, and (d) the retrieved cloud height, over the $5^\circ \times 5^\circ$ area over Wisconsin at 2100 UTC, 28 October 1986.

The computed mean effective sizes, however, have not been validated against aircraft observations, because the aircraft data that are properly collocated and coincident with the satellite overpass were not available. In Figure 13(c), the retrieved optical depth ranges between 0 and 8. The map of the optical depth matches that of the Ch. 4 brightness temperature shown in Figure 12. In Figure 13(d), the distribution of cloud heights is determined from the distribution of cloud temperature using the averages of the 2100 UTC soundings data at Plattville and Green Bay, Wisconsin (Starr and Wylie, 1990). The cloud heights range between 6 and 11 km. The distribution of cloud height agrees with that of cloud temperature [Figure 13(a)] and mean effective ice crystal size [Figure 13(b)].

The preceding results are compared with results presented by Minnis et al. (1990b), who also derived the distributions of cloud height and cloud optical depth, using both the AVHRR visible and IR channel data over the same area and for the same time period. Minnis et al. (1990b) derived the optical depth directly from the Ch. 1 bidirectional reflectances based on radiative transfer calculations (Takano and Liou, 1989b). The present removal-retrieval scheme, however, derives the optical depth based on the parameterization of the Ch. 4 emissivity. Minnis et al. (1990b) showed that the optical depth ranges between 0 and 5 for most of the area. Over the major cloudy areas near the northwest corner and at about 45°N and 89°W , the optical depth is shown to be greater than 5. The distribution of the optical depth from the present removal-retrieval scheme agrees reasonably well with that presented by Minnis et al. (1990b). The present results show more detailed features, however. The distribution of cloud height derived by Minnis et al. (1990b) is between 7 and 11 km for most areas. It should be noted that the cloud heights presented by Minnis et al. (1990b) are the cloud-center heights, which were derived through empirical formulas that relate cloud temperature and cloud-top temperature. In the present scheme, however, the retrieved cloud height is close to the cloud-top height for thicker

clouds. Therefore, over most of the cloudy areas, the cloud heights determined from the present scheme are slightly higher than those presented by Minnis et al. (1990b).

Finally, for verifications and comparisons, Table 4 lists the retrieved values of cloud temperature, mean effective ice crystal size, cloud height, and optical depth from the present scheme. Also listed are the cloud temperature and midcloud height derived from lidar and sounding data, and the optical depth derived from the GOES data (Minnis et al. 1990a). Comparisons are made near the three FIRE-I-IFO stations whose locations are identified in Figure 12: Madison (MAD, 43.1°N, 89.4°W), Fort McCoy (FMC, 43.9°N, 90.8°W), and Wausau (WAU, 45.0°N, 89.7°W). The retrieved values from the present scheme are based on the average of all pixels within a 1° x 1° area around each station. Cloud temperatures and cloud heights at all three stations determined from the present scheme agree reasonably well with those from lidar data (Sassen et al., 1990). The differences in cloud temperature and cloud height are less than 4.2 K and 0.5 km, respectively. These differences may be caused by the effect of the vertical inhomogeneity within cirrus clouds. The optical depths inferred from the present scheme are slightly larger than those derived from the GOES data by about 0.1. It is noted that Minnis et al. (1990a) derived their optical depths based on a cirrostratus microphysical model with a mean effective size of about 41.5 μm . The mean effective size retrieved from the present study is between 50 and 60 μm . In summary, the retrieved cloud parameters agree reasonably well with the observations and with results computed from different techniques.

4.3 Retrievals over a 20° x 30° Area

We have performed the daytime retrieval of cirrus cloud parameters covering the midwestern United States for the time period 2100 UTC, 28 October 1986. Figure 14 shows the display of Ch. 4 brightness temperatures. The area covered is from 30° to 50°N and from 80° to 110°W. It is evident that clouds are present

over the Great Lakes region (outlined by dots over the northeast corner) and the southeast United States. The rest of the area is relatively clear. For comparison, Figure 15 displays the AVHRR Ch. 1 satellite imagery based on HRPT (High-Resolution Pixel Transmission) data over the same area and time period.

The data domain is divided into 70 $3^\circ \times 3^\circ$ boxes. For each box, we compute a single set of average sun-satellite geometrical parameters for the purpose of correlating Chs. 1 and 3 reflectances based on radiative transfer calculations. The variations in the solar zenith angle, satellite zenith angle, and relative azimuthal angle for pixels within each box are less than 3° , 8° , and 2° , respectively. Radiative transfer calculations show that these angular variations produce negligible variations in the Chs. 1 and 3 reflectances. Each box is further divided into nine $1^\circ \times 1^\circ$ mini-boxes. The clear/cloud detection program is applied to all pixels in each mini-box to obtain the Ch. 1 effective surface albedo from the mode of the histogram of all Ch. 1 clear reflectances in the box. We then apply the removal-retrieval scheme to cloudy pixels in each mini-box, utilizing a pair of Chs. 3 and 4 thermal infrared clear radiances for each mini-box. If no clear pixels are detected within the mini-box, the clear radiances of a neighboring box are used. The averages of Green Bay and Plattville soundings at 2100 UTC are employed to compute the transmittances for clear atmospheres.

Figures 16(a)-(c) display the retrieved cirrus cloud temperatures, optical depths, and mean effective sizes, respectively. Over the northern Great Lakes region, cloud temperatures are lower (~ 230 K), with larger pockets of cold cirrus (< 230 K) than over the southeastern corner. Moreover, the corresponding cloud optical depths are larger than 8 over the Great Lakes region. Small mean effective sizes ($< 50 \mu\text{m}$) are found near the northern edge of Lake Superior. These retrieval results are consistent with the high-resolution satellite cloud picture shown in Figure 15. To the northeast and east of the Great Lakes, the

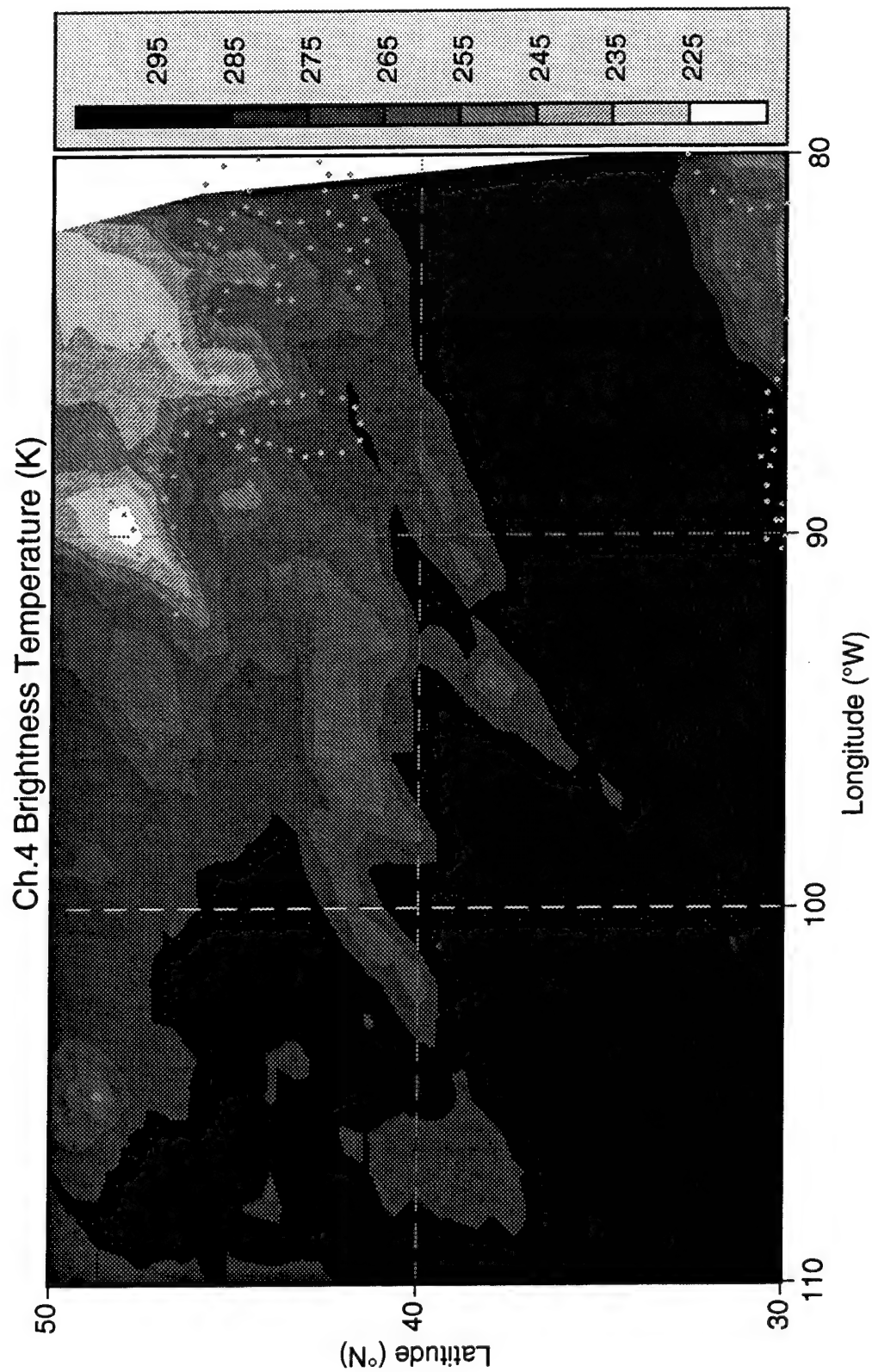


Fig 14. Display of the Ch. 4 brightness temperatures over the midwestern United States at 2100 UTC, 28 October, 1986.

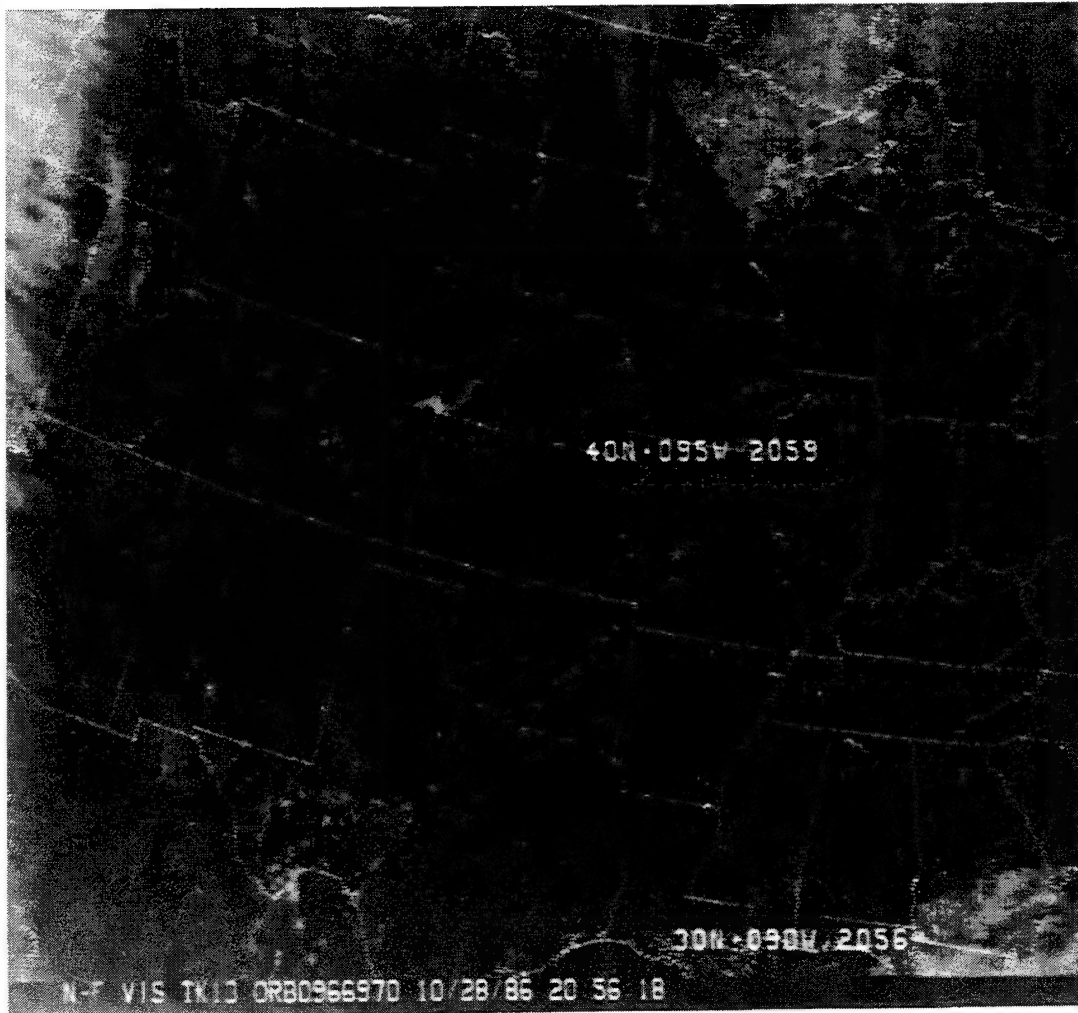


Fig 15. The AVHRR Ch. 1 satellite imagery over the midwestern United States at 2100 UTC, 28 October 1986.

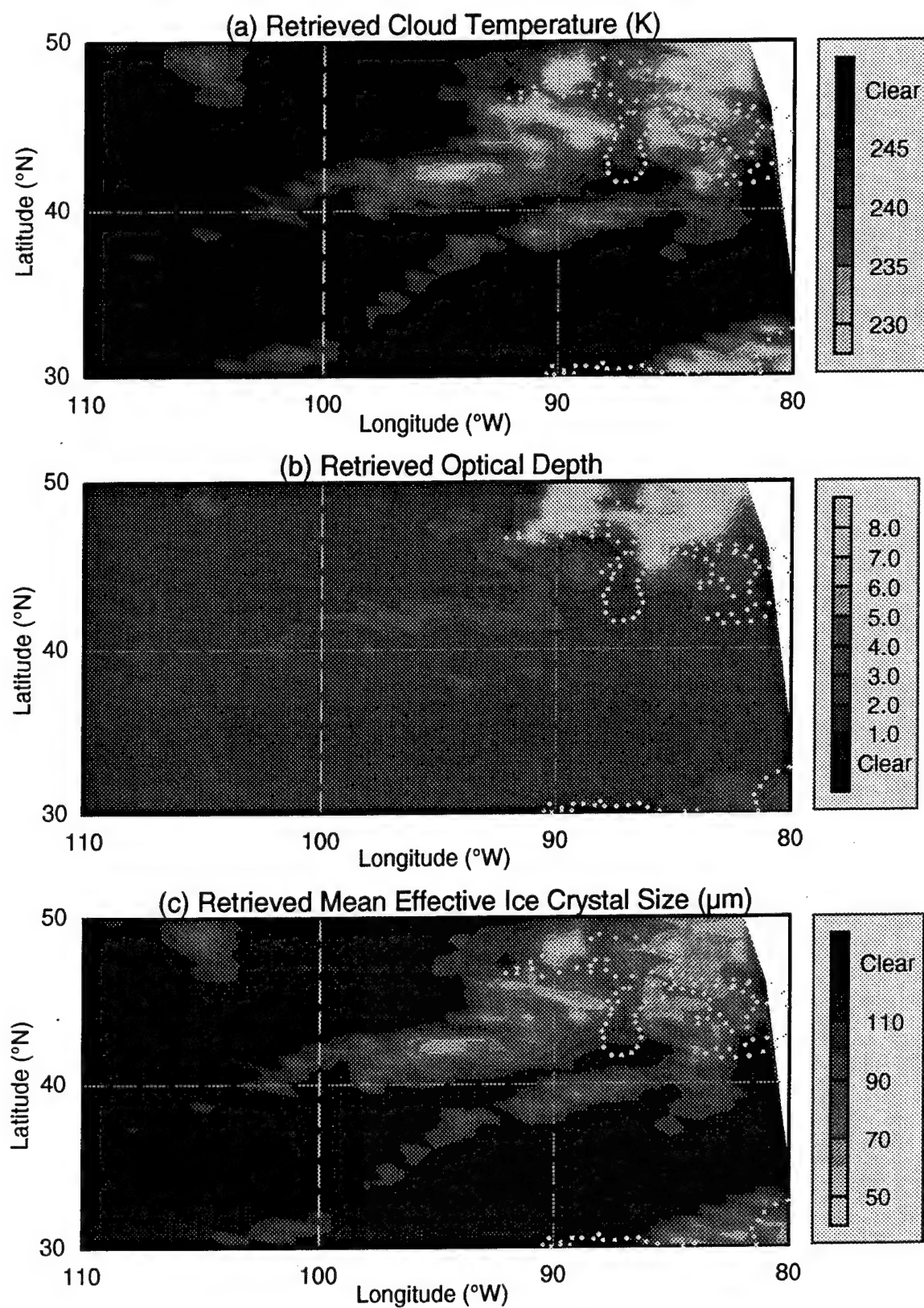


Fig 16. Display of (a) retrieved cloud temperature, (b) the retrieved optical depth, and (c) the retrieved mean effective sizes, over the area shown in Fig. 8.

Table 4. Cirrus cloud temperature, mean effective ice crystal size, cloud height, and optical depth determined from the present retrieval program.

	$T_c(K)$		$D_e(\mu m)$	$z(km)$		τ	
	present	lidar*	present	present	lidar*	present	GOES*
WAU	226.5	230.7	57.1	9.5	9.0	1.54	1.43
FMC	229.7	226.5	61.3	9.1	9.5	1.5	1.41
MAD	225.6	228.1	53.9	9.6	9.3	0.6	0.56

*after Minnis et al. (1990a).

area is mostly covered with clouds. The visible satellite cloud picture indicates that the same area is relatively dark, due probably to the large solar zenith angle over that area ($\sim 80^\circ$). Moreover, the Ch. 4 brightness temperatures are less than 245 K and the brightness temperature difference between Chs. 4 and 5 are between 2 and 3 K, indicating the presence of thick cirrus over that region. Although it is possible that low-level clouds could have been present, reliable schemes for detecting multi-layer cloud systems are yet to be developed to identify this situation.

5. VERIFICATION USING FIRE-II-IFO MEASUREMENTS

5.1 Data Sources

The FIRE-II-IFO was carried out near Coffeyville, Kansas, during November and December, 1991. One of the objectives of this field experiment was to quantify the capabilities and limitations of methods for retrieving physical and optical cirrus cloud properties from satellite observations. During the latter part of November and the first part of December, 1991, a total of 11 cirrus days was observed. For all these cases, we have reviewed the available satellite data and lidar measurements as well as examined the temporal differences between the satellite overpass time and the sampling time of the sounding system. We find that around 2100 UTC on both 26 November and 5 December, there were well defined cirrus cloud layers over the Coffeyville area and that the temporal differences between the satellite overpasses and replicator measurements are less than 30 minutes. Thus, we have focused on these two dates for the retrieval analyses and verifications.

For the retrieval of cirrus cloud properties, high-resolution (HRPT) AVHRR data from NOAA-11 satellite are used. This satellite has nominal equator crossing times of 0140 and 1340 LST. The AVHRR is comprised of five channels: 0.63, 0.8, 3.7 (NIR), 10.9 (IR), and 12 μm . The NIR and IR radiances were calculated from the raw counts provided in the NOAA-1B data stream using the nominal calibration (Kidwell 1991) and from the nonlinearity corrections described by Weinreb et al. (1990). The visible channel radiances were calculated using the instrument degradation correction function provided by Whitlock et al. (1990).

Balloon-borne formvar (polyvinyl formal) ice crystal replicators were launched during FIRE-II-IFO to measure the "vertical profiles" (in a Lagrangian sense) of cirrus microphysical properties, with emphasis on the detection of small ice particles. Schaefer (1941) first developed the formvar replication

technique to capture and preserve detailed features of snowflakes, using a solution of formvar dissolved in ethylene dichloride. Particles falling onto a solution-coated slide or filmstrip are enveloped by fluid, forming a detailed replica of the particle when the solvent evaporates and the plastic hardens. The use of formvar replication on a balloon-borne instrument, i.e. a "replicator sonde", was developed by Magono and Tazawa (1966) to study the vertical distribution of snow crystals up to 500 mb level in a snow cloud. The fundamental design of the ice crystal replicator employed in FIRE-II-IFO was based on the prototype developed by Magono and Tazawa, with modifications to improve the data quality and to allow the instrument to collect data in high and cold cirrus clouds.

Replicator launches were timed to coincide with satellite overpasses and during the time periods when ground-based remote sensors and aircraft were operating. The replicators were launched together with the NCAR-CLASS and then tracked and retrieved by an automobile using the radio direction-finding (RDF) equipment. The balloon size and inflation were chosen to deliver an ascent rate of about 5 m/sec and to burst at 11-13 km altitude, after which the train descended on a parachute. More comprehensive discussions on the replicator data have been presented by Heymsfield and Miloshevich (1993). High resolution radiosonde data and position coordinates were obtained from the NCAR-CLASS.

5.2 Results and Discussions

As described previously, the Fire-II-IFO over Coffeyville was carried out during November-December 1991 with a total number of 11 observed cirrus days (November 13, 17, 22, 25, 26, 27, 28, 29, 30, and December 5 and 6). Based on inspection of the available AVHRR data, replicator measurements, NCAR-CLASS sounding data, and surface broadband radiative flux measurements, we find that the data collected during 5 December are most appropriate for the present retrieval analyses and verifications for the following reasons. First, on that

date, a layer of well defined cirrus cloud was present over Coffeyville, so that the retrieval scheme, which was principally designed to retrieve the single-layer cloud properties, can be directly applied to the satellite data. Second, the temporal differences between the satellite overpass time and the replicator sampling time are small. The two data sets are therefore closely coincident and can be collected in a Lagrangian sense. This part will be discussed further for each case. Finally, the satellite viewing angles are also small ($< 30^\circ$). This condition guarantees that the size for each pixel is small, so that the effects of cloud horizontal inhomogeneity on the analysis can be minimized.

On 5 December, the sky was clear at sunrise and not very cold. A rapid influx of light cirrus (Spissatus) was observed from the west during the morning. Coverage and density of cirrus increased through the day. Aircraft and ground-based sensors estimated cloud bases in the 10 km range, with tops extending to around 13 km. During the late afternoon, multi-layered features covered the sky, with all stations in Kansas reporting high level clouds. No low or middle level clouds passed over Coffeyville, but some low clouds were visible in the distant southern sky during the afternoon.

Figures 17(a)-(c) show the distribution of Ch. 4 brightness temperatures, and the retrieved optical depths and mean effective ice crystal sizes over the $0.5^\circ \times 1.0^\circ$ domain ($36.75^\circ - 37.25^\circ$ N; $94.8^\circ - 95.8^\circ$ W) at 2100 UTC, 5 December 1991, respectively. The symbol "+" denotes the location of Coffeyville. It is noted that almost the whole domain was covered with cirrus clouds. The distribution of the retrieved optical depths closely match that of the Ch. 4 brightness temperature. The cloud optical depth northeast of Coffeyville and near the southern boundary of the domain is larger than 3. However, the distribution of mean effective ice crystal sizes show no correlation with that of the Ch. 4 brightness temperature. Generally, the mean effective size increases from the south toward the north. The reliability of these retrieval

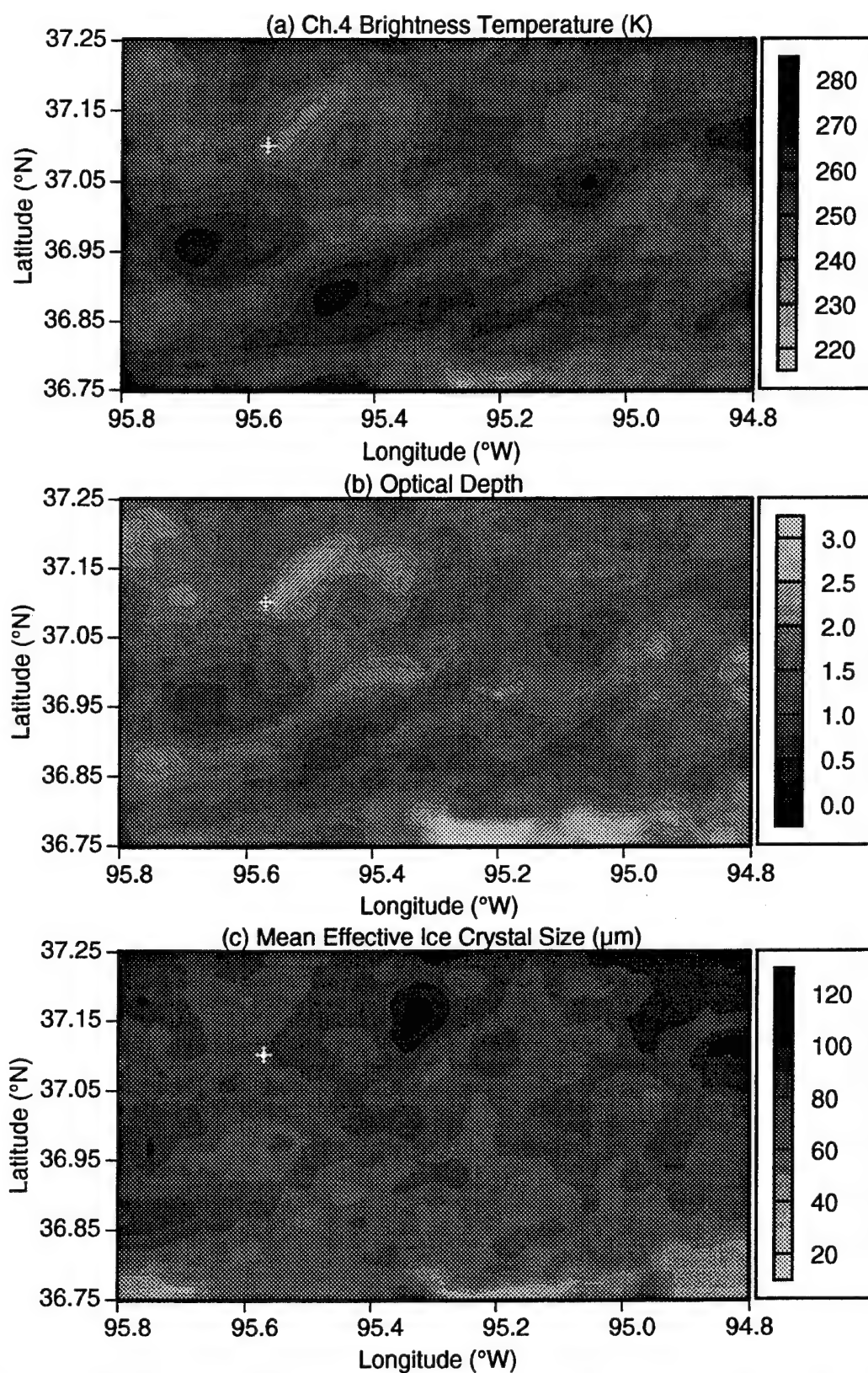


Fig 17. Display of (a) AVHRR Ch. 4 brightness temperature, (b) the retrieved optical depth, and (c) the retrieved mean effective ice crystal size over a $0.5^\circ \times 1.0^\circ$ area around Coffeyville, Kansas (denoted by the symbol "+"), at 2108 UTC, 5 December 1991.

results can only be confirmed by comparing with independently derived observational data.

Figures 18(a)-(e) show the ice crystal size distributions derived from the replicator data at five selected height levels between the cloud base and cloud top. Near the cloud top (~ 13 km), the cirrus cloud is composed of small quasi-spherical particles ($L < 100 \mu\text{m}$). The smallest ice crystals that the replicator can measure are on the order of $5 \mu\text{m}$. In the middle part of the cloud (9.8 - 12.0 km), there are columns, bullets, plates, and irregular particles. The size distributions become wider and more large particles appear in the lower part of the cloud. Near the 9.77-km level, the size distribution is bimodal, where the larger mode is presumably due to the presence of large particles falling out from higher levels. Finally, near the cloud base (~ 9.6 km), there are only partially sublimated, irregularly shaped ice crystals.

Because clouds are horizontally inhomogeneous, collocation and coincidence of the satellite data and replicator measurements in a Lagrangian sense are required for validation of the retrieval results. Figure 19 shows the geographical coordinates of the replicator at various times after launching. The replicator was launched at 2045 UTC and reached the cloud base and top at 2113 and 2125 UTC, or 5 and 17 minutes after the satellite overpass, respectively. These temporal differences are relatively small compared to the life time of cirrus clouds, which is on the order of several hours. To collocate the two data sets, we must determine the precise position of the cloudy region under the satellite overpass that was sampled by the replicator. In Figure 19, the open and closed circles denote the coordinates of the sounding system when it reached the cloud base and top, respectively. Using the cloud-level windspeed and wind direction data recorded by the NCAR-CLASS sounding system, we determine that at the time of satellite overpass the cloud associated with the replicator measurements was located at a position denoted by "x". This point

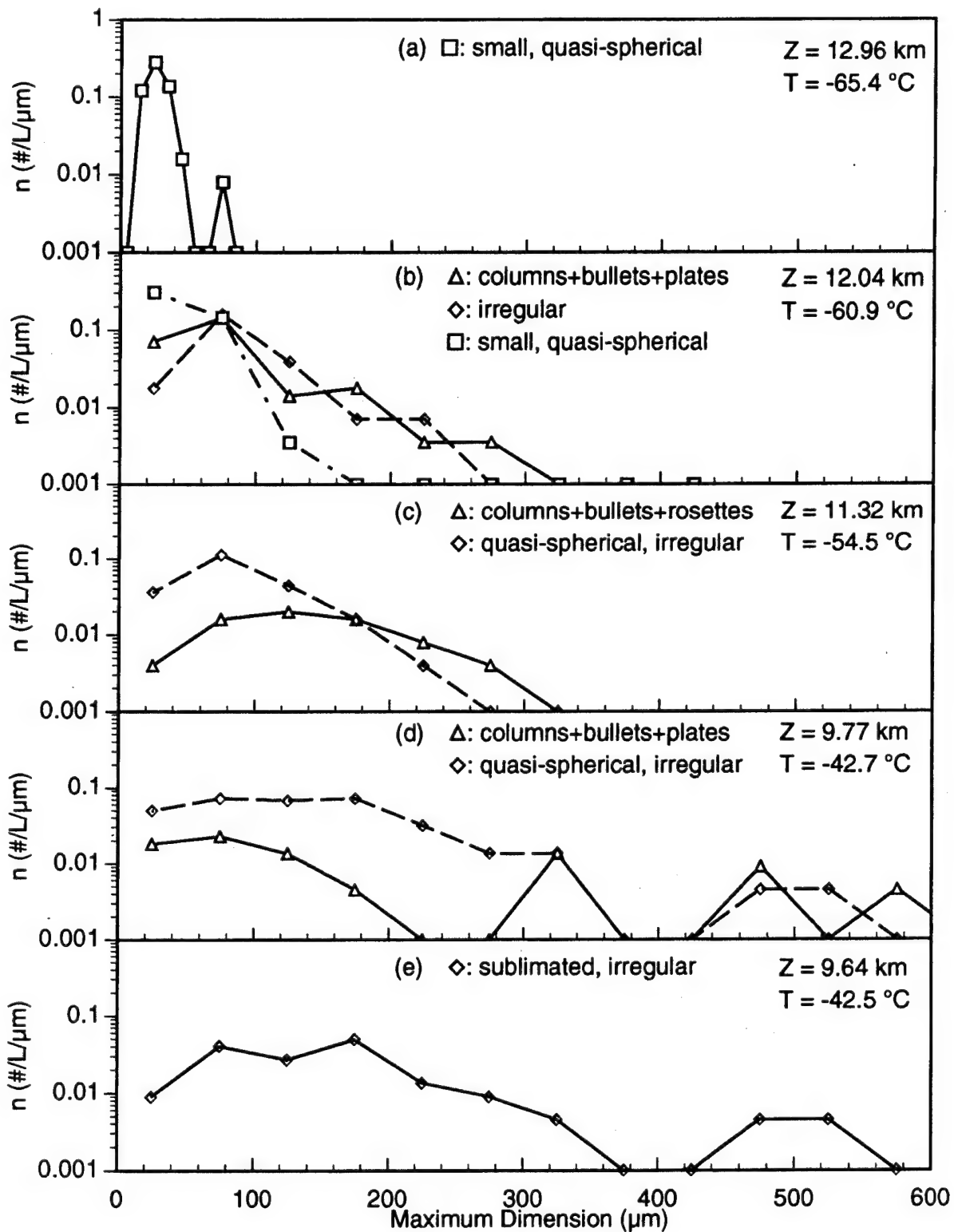


Fig 18. Ice crystal size distributions derived from the replicator data at five selected height levels within the cloud, which was sampled between 2113 and 2125 UTC, 5 December 1991.

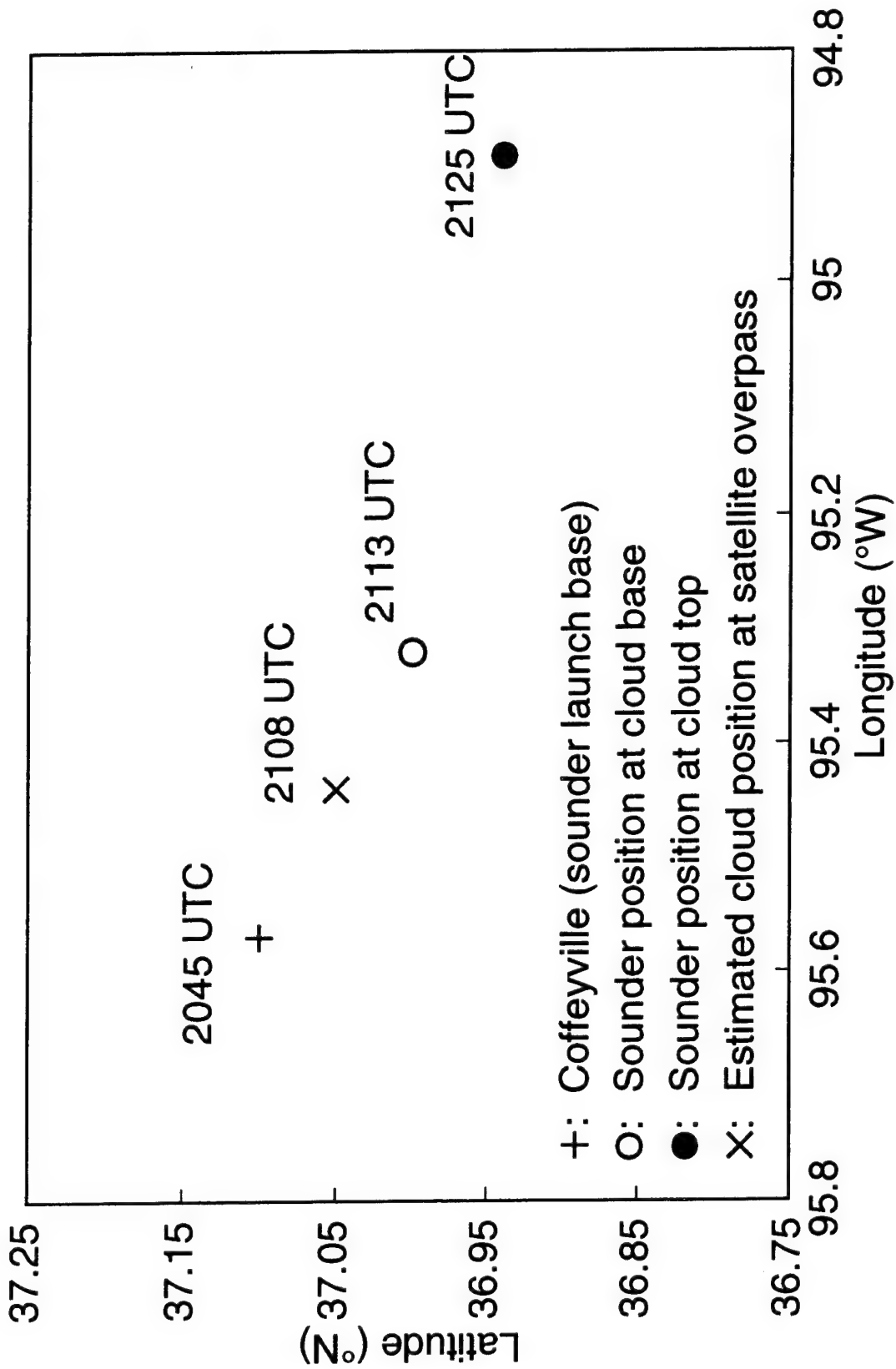


Fig 19. Geographical coordinates of the replicator at various times after launching on 5 December 1991.

near Coffeyville was upwind of the sounder positions at the cloud base and top, because the satellite overpass was before the replicator sampling. Since the coordinates of this point are subject to uncertainties in the wind data, an area of $0.05^\circ \times 0.2^\circ$ around this point is subsequently selected for the verification study.

Figures 20(a)-(b) show the averaged retrieval results within the $0.05^\circ \times 0.2^\circ$ domain along with sounding measurements. Figure 20(a) displays the temperature and relative humidity profiles obtained from the NCAR-CLASS sounding system between 2045 and 2129 UTC. The cloud base and top heights derived from the replicator sounding are 9.5 and 13 km, respectively. The relative humidity sharply increases with height near the cloud base and decreases upward above 10 km. The mean retrieved cloud temperature is 212 K, which is the average of 81 pixels within the $0.05^\circ \times 0.2^\circ$ area. The standard deviation is 3 K, revealing that cloud temperatures are relatively uniform within the retrieval domain. Moreover, the mean cloud height determined from the temperature sounding is 11.5 km, which is within the observed cloud boundaries. It should be noted that the mean Ch. 4 brightness temperature is 255 K, much higher than the mean retrieved cloud temperature. If this temperature were used to retrieve the cloud height, the error will be on the order of 6 km.

Figure 20(b) shows the vertical distribution of mean effective ice crystal sizes computed from the replicator data. The mean effective size is $15 \mu\text{m}$ near the cloud top and increases to $135 \mu\text{m}$ near the cloud base. From these values, we determine the vertically averaged mean effective ice crystal size to be $97.3 \mu\text{m}$, as shown in Figure 20(b) by the solid vertical bar. This size is the sum of the mean effective ice crystal size at a given level weighed by the number density at that level normalized by the total number density. The retrieved mean effective size is $88.7 \mu\text{m}$, which differs from the replicator value by less than $10 \mu\text{m}$. On the bottom scale of Figure 20(b) are shown the replicator-derived and

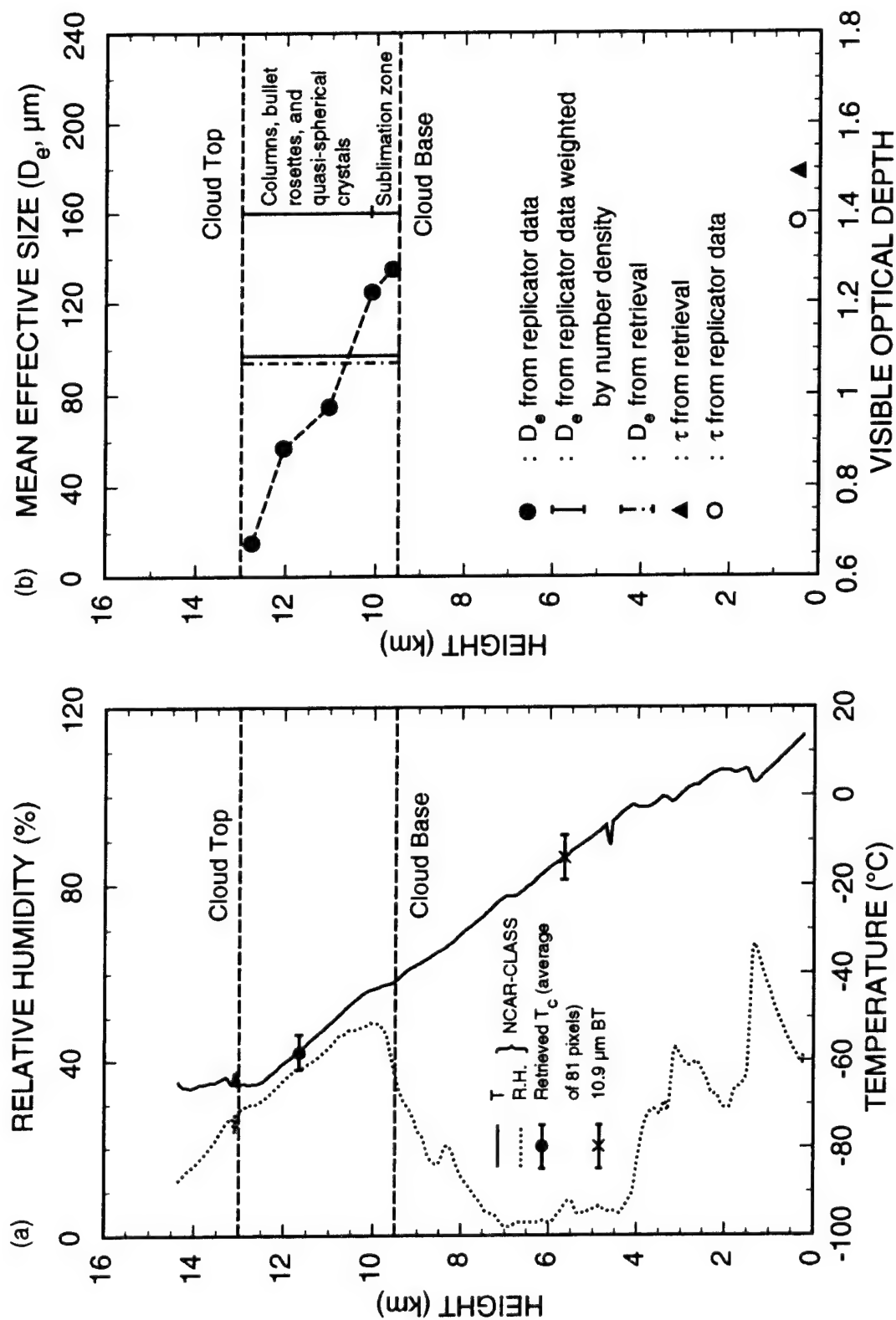


Fig 20 (a). Temperature and humidity profiles obtained from the NCAR-CLASS sounding system on 5 December 1991. Overlapped with the temperature profile are the mean retrieved cloud temperature and mean Ch. 4 brightness temperature over a $0.05^\circ \times 0.2^\circ$ domain around Coffeyville. (b). Display of the replicator-derived mean effective sizes at the selected height levels, their vertical average, and the retrieved value. Also shown on the bottom scale are the optical depths derived from the replicator data and from the retrieval.

the retrieved optical depths, which are 1.38 and 1.49, respectively. The differences in the retrieved and replicator-derived mean effective size and optical depth could well be due to the small time difference between satellite pass and replicator sounding.

6. CONCLUSIONS

A removal-retrieval technique based on radiative transfer parameterizations has been developed for inferring cirrus cloud parameters during local daytime. This scheme uses radiance data of AVHRR 3.7 and 10.9 μm channels to simultaneously determine cirrus temperature, mean effective ice crystal size, and optical depth. During the local daytime, the 3.7 μm (Ch. 3) solar component is removed by using the correlation between Ch. 1 (0.63 μm) and Ch. 3 solar reflectances. This correlation is derived from radiative transfer calculations.

We have carried out sensitivity studies on the accuracy of the removal scheme. Overall, for optical depths larger than 1, the maximum percentage error in the 3.7 μm solar component is less than 10%. Moreover, we have performed retrievals over a $1^\circ \times 1^\circ$ area west of Fort McCoy, Wisconsin, using the AVHRR data collected at 2100 UTC, 28 October 1986. The distribution of Ch. 4 brightness temperature over this area shows distinct clear regions. Based on the retrieved cloud temperature, several cold cirrus-generating regions are shown along with large areas of warm, stable, and dissipating cirrus clouds that are present to the north and east of the cirrus-forming regions. Significant differences are evident for the patterns of the retrieved optical depth and cloud temperature. The retrieved mean effective ice crystal sizes range from 30 to 90 μm , which appear to be consistent with the observed values.

We have applied the removal-retrieval scheme to retrieve cirrus parameters over a $5^\circ \times 5^\circ$ area, using the same daytime data set collected on 28 October 1986. The retrieved cloud temperatures and cloud heights compare reasonably well with the results presented by other researchers using different methods and with available lidar and aircraft measurements. We have also carried out the mapping of cirrus cloud parameters over the midwestern United States. The distributions of the retrieved cirrus cloud parameters are consistent with the satellite cloud picture based on the high-resolution AVHRR Ch. 1 reflectances.

Moreover, verifications of the retrieved cirrus optical depth and ice crystal sizes have been performed using balloon-borne replicator and sounding data obtained during FIRE-II-IFO. We have taken the advantage that the balloon-borne replicator data can provide a nearly continuous vertical record of ice crystal size distributions in a Lagrangian sense. An analytical method has been developed to derive the optical depth and the mean effective ice crystal size from the replicator data, taking into account the effects of different shapes, including quasi-spherical, irregular, and hexagonal ice crystals. Moreover, we apply the retrieved cloud properties to the computation of surface radiative fluxes using a radiative transfer program that involves a consistent representation of cloud fields and compare the computed values with data measured from ground-based radiometers.

We have focused on the case of 5 December. On that date, a well defined cirrus layer was present over the Coffeyville area and the temporal differences between the satellite overpass and the replicator sampling are small. The two data sets are closely coincident and can be collocated in a Lagrangian sense. In each case, we first perform retrievals over a $0.5^\circ \times 1.0^\circ$ region around the Coffeyville area and obtain the distribution of cloud optical depth and mean effective size. We then determine the precise position of the cloudy region that was sampled by the replicator under the satellite overpass. A small area around this position is subsequently chosen and the mean retrieved cloud parameters of this domain are compared with those derived from the replicator and sounding data. We show that the retrieved cirrus cloud temperature, mean effective size, and optical depth closely match with the values determined from sounding and replicator data. Differences in the retrieved and replicator-derived values of the cloud parameters could be a result of the small temporal differences between the satellite pass and replicator sounding.

REFERENCES

- Allen, R.C., P.A. Durkee, and C.H. Wash, 1990: Snow/Cloud discrimination with multispectral satellite measurements. *J. Appl. Sci.*, 29, 994-1004.
- Arking, A., and J.D. Childs, 1985: Retrieval of cloud cover parameters from multispectral satellite images. *J. Climate Appl. Meteor.*, 23, 322-333.
- Auer, A.H., and D.L. Veal, 1970: The dimension of ice crystals in natural clouds. *J. Atmos. Sci.*, 27, 919-926.
- Baum, B.A., T. Uttall, M. Peolott, T.P. Ackerman, J.M. Alvarez, J. Intrieri, D. O'C Starr, J. Titlow, V. Tovinkere, and E. Clothiaux, 1994: Satellite remote sensing of multiple cloud layres. Submitted to the *J. Atmos. Sci.*, FIRE Special issue.
- Bunting, J.T., and K.R. Hardy, 1974: Cloud identification and characterization from satellites. *Satellite Sensing of a Cloudy Atmosphere: Observing the Third Planet*. A. Henderson-Sellers, Ed., Taylor and Francis, 203-240.
- Chou, M.D., 1991: The derivation of cloud parameters from satellite-measured radiances for use in surface radiation calculations. *J. Atmos. Sci.*, 48, 1549-1559.
- Dudhia, A., 1989: Noise characteristics of the AVHRR infrared channels. *Int. J. Remote Sens.*, 10, 637-644.
- Handbook of Geophysics and the Space Environment*, 1985: Air Force Geophysics Laboratory, Chap. 18.
- Heymsfield, A., 1975: Cirrus uncinus generating cells and the evolution of cirriform clouds. Part I: Aircraft observations of the growth of the ice phase. *J. Atmos. Sci.*, 32, 799-808.
- Heymsfield, A.J., and L.M. Miloshevich, 1993: Overview of microphysics and state parameters measurements from FIRE-II. FIRE Cirrus Results, Proceedings of a conference held at Breckenbridge, Co., June 14-17, 1-4.
- Heymsfield, A.J., and C.M.R. Platt, 1984: A parameterization of the particle size spectrum of ice clouds in terms of the ambient temperature and the ice water content. *J. Atmos. Sci.*, 41, 846-855.
- Heymsfield, A.J., K.M. Miller, and J.D. Spinhirne, 1990: The 27-28 October 1986 FIRE IFO cirrus case study: Cloud microstructure. *Mon. Wea. Rev.*, 118, 2313-2328.
- Kidwell, K.B., 1991: NOAA Polar Orbiter Data Users Guide. NOAA/NESDIS, Washington, D.C., Ch. 3.
- Kleespies, T.J., 1993: Retrieval of cloud parameters by multiple observations in the near-infrared under conditions of varying solar illumination. *SPIE's OE/Aerospace and Remote Sensing Symposium*, 12-16 April 1993, Orlando, Florida (Proceeding in press).
- Liou, K.N., 1980: *An Introduction to Atmospheric Radiation*, Academic Press, New York, 392 pp.

- Liou, K.N., 1986: Influence of cirrus clouds on weather and climate processes: A global perspective. *Mon. Wea. Rev.*, 114, 1167-1199.
- Liou, K.N., 1992: *Radiation and Cloud Processes in the Atmosphere*. Oxford University Press, New York, 487 pp.
- Liou, K.N., S.C. Ou, Y. Takano, F.P.J. Valero, and T.P. Ackerman, 1990: Remote sounding of the tropical cirrus cloud temperature and optical depth using 6.5 and 10.5 μm radiometers during STEP. *J. Appl. Meteor.*, 29, 716-726.
- Magono, C., and S. Tazawa, 1966: Design of "snow crystal sondes." *J. Atmos. Sci.*, 23, 618-625.
- Minnis, P., D.F. Young, K. Sassen, J.M. Alvarez, and C.J. Grund, 1990a: The 27-28 October 1986 FIRE IFO cirrus case study: Cirrus parameter relationships derived from satellite and lidar data. *Mon. Wea. Rev.*, 118, 2402-2425.
- Minnis, P., P.W. Heck, and E.F. Harrison, 1990b: The 27-28 October 1986 FIRE IFO cirrus case study: Cloud parameter fields derived from satellite data. *Mon. Wea. Rev.*, 118, 2426-2446.
- Minnis, P., K.N. Liou, and Y. Takano, 1993a: Inference of cirrus cloud properties using satellite-observed visible and infrared radiances. Part I: Parameterization of radiance fields. *J. Atmos. Sci.*, 50, 1279-1304.
- Minnis, P., P.W. Heck, and D.F. Young, 1993b: Inference of cirrus cloud properties from satellite-observed visible and infrared radiances. Part II: Verification of theoretical cirrus radiative properties. *J. Atmos. Sci.*, 50, 1305-1322.
- Ou, S.C., K.N. Liou, W.M. Gooch, and Y. Takano, 1993: Remote sensing of cirrus cloud parameters using advanced very-high-resolution radiometer 3.7- and 10.9- μm channels. *Appl. Opt.*, 32, 2171-2180.
- Rossow, W.B., and R.A. Schiffer, 1991: ISCCP cloud data products. *Bull. Amer. Meteor. Soc.*, 72, 2-20.
- Sassen, K., C.J. Grund, J.D. Spinhirne, M.M. Hardesty, and J.M. Alvarez, 1990: The 27-28 October 1986 FIRE IFO cirrus case study: A five lidar overview of cloud structure and evolution. *Mon. Wea. Rev.*, 118, 2288-2311.
- Saunders, R.W., and K.T. Kriebel, 1988: An improved method for detecting clear sky and cloudy radiances from AVHRR data. *Int. J. Remote Sensing*, 9, 123-150.
- Schaefer, V., 1941: A method for making snowflake replicas. *Science*, 93, 239-240.
- Starr, D.O.C., and D.P. Wylie, 1990: The 27-28 October 1986 FIRE cirrus case study: Meteorology and clouds. *Mon. Wea. Rev.*, 118, 2259-2287.
- Staylor, W.F., 1990: Degradation rates of the AVHRR visible channel for the NOAA 6, 7, and 9 spacecraft. *J. Atmos. Ocean Tech.*, 7, 411-423.
- Sutherland, R.A., 1986: Broadband and spectral emissivities (2-18 μm) of some natural soils and vegetation. *J. Atmos. Ocean. Technol.*, 3, 199-202.

- Takano, Y., and K.N. Liou, 1989a: Solar radiative transfer in cirrus clouds. Part I: Single scattering and optical properties of hexagonal ice crystals. *J. Atmos. Sci.*, 46, 3-19.
- Takano, Y., and K.N. Liou, 1989b: Solar radiative transfer in cirrus clouds. Part II: Theory and computation of multiple scattering in an anisotropic medium. *J. Atmos. Sci.*, 46, 20-36.
- Thekaekara, M.P., 1974: Extraterrestrial solar spectrum, 300-6100 Å at 1 Å intervals. *Appl. Opt.*, 13, 518-522.
- Weinreb, M., G. Hamilton, and S. Brown, 1990: Nonlinearity corrections in calibration of Advanced Very High Resolution Radiometer infrared channels. *J. Geophys. Res.*, 95, 7381-7388.
- Whitlock, C.H., W.F. Staylor, J.T. Suttles, G.L. Smith, and others, 1990: AVHRR and VISSR satellite instrument calibration results for both cirrus and marine stratocumulus IFO periods. NASA CP 3083, 141-146.
- Wielicki, B.A., J.T. Suttles, A.J. Heymsfield, R.M. Welch, J.D. Spinhirne, M.-L.C. Wu, D. O'C. Starr, L. Parker, and R.F. Arduini, 1990: The 27-28 October 1986 FIRE IFO Cirrus Case Study: Comparison of radiative transfer theory with observations by satellite and aircraft. *Mon. Wea. Rev.*, 118, 2356-2376.